The Role of the Most Luminous Obscured AGNs in Galaxy Assembly at $z \sim 2$

Duncan Farrah[1], Sara Petty[2], Brian Connolly[3], Andrew Blain[4], Andreas Efstathiou[5], Mark Lacy[6], Daniel Stern[7], Sean Lake[8], Tom Jarrett[9], Carrie Bridge[7], Peter Eisenhardt[7], Dominic Benford[10], Suzy Jones[11], Chao-Wei Tsai[8], Roberto Assef[12], Jingwen Wu[13], and Leonidas Moustakas[7]

[1] Department of Physics, Virginia Tech, Blacksburg, VA 24061, USA
[2] Green Science Policy Institute, Berkeley, CA 94709, USA
[3] Cincinnati Children's Hospital Medical Center, 3333 Burnet Avenue, Cincinnati, OH 45229, USA
[4] Department of Physics and Astronomy, University of Leicester, Leicester LE1 7RH, UK
[5] School of Sciences, European University Cyprus, Diogenes Street, Engomi, 1516 Nicosia, Cyprus
[6] National Radio Astronomy Observatory, 520 Edgemont Road, Charlottesville, VA 22903, USA
[7] Jet Propulsion Laboratory, California Institute of Technology, 4800 Oak Grove Drive, Pasadena, CA 91109, USA
[8] Physics and Astronomy Department, University of California, Los Angeles, CA 90095, USA
[9] Department of Astronomy, University of Cape Town, 7700 Rondebosch, Capetown 7700, South Africa
[10] Observational Cosmology Lab., Code 665, NASA at Goddard Space Flight Center, Greenbelt, MD 20771, USA
[11] Department of Space, Earth, and Environment, Chalmers University of Technology, Onsala Space Observatory, SE-43992 Onsala, Sweden
[12] Núcleo de Astronomía de la Facultad de Ingeniería, Universidad Diego Portales, Av. Ejército Libertador 441, Santiago, Chile
[13] National Astronomical Observatories, Chinese Academy of Sciences, 20A Datun Road, Chaoyang District, Beijing, 100012, China

Abstract

We present *Hubble Space Telescope* WFC3 F160W imaging and infrared spectral energy distributions for 12 extremely luminous, obscured active galactic nuclei (AGNs) at $1.8 < z < 2.7$ selected via "hot, dust-obscured" mid-infrared colors. Their infrared luminosities span $(2–15) \times 10^{13} L_{\odot}$, making them among the most luminous objects in the universe at $z \sim 2$. In all cases, the infrared emission is consistent with arising at least for the most part from AGN activity. The AGN fractional luminosities are higher than those in either submillimeter galaxies or AGNs selected via other mid-infrared criteria. Adopting the G, M_{20}, and A morphological parameters, together with traditional classification boundaries, infers that three-quarters of the sample are mergers. Our sample does not, however, show any correlation between the considered morphological parameters and either infrared luminosity or AGN fractional luminosity. Moreover, the asymmetries and effective radii of our sample are distributed identically to those of massive galaxies at $z \sim 2$. We conclude that our sample is not preferentially associated with mergers, though a significant merger fraction is still plausible. Instead, we propose that our sample includes examples of the massive galaxy population at $z \sim 2$ that harbor a briefly luminous, "flickering" AGN and in which the G and M_{20} values have been perturbed due to either the AGN and/or the earliest formation stages of a bulge in an inside-out manner. Furthermore, we find that the mass assembly of the central black holes in our sample leads the mass assembly of any bulge component. Finally, we speculate that our sample represents a small fraction of the immediate antecedents of compact star-forming galaxies at $z \sim 2$.

Key words: galaxies: evolution – galaxies: high-redshift – galaxies: starburst – quasars: general

1. Introduction

Active galactic nuclei (AGNs) play a fundamental role in galaxy assembly. AGNs signpost the relatively brief periods in a galaxy's lifetime when the central supermassive black hole is accreting rapidly, during which time the black hole likely assembled the bulk of its mass (Draper & Ballantyne 2012; Treister et al. 2012). There is also a deep connection between AGN activity and star formation rates at all redshifts. The most striking evidence for this connection is the similar cosmological evolution of AGNs and star formation; the optical luminosity function of quasars plateaus in the range $2 < z < 3$ (e.g., Richards et al. 2006; Delvecchio et al. 2014), while the comoving star formation rate density also peaks at $z \sim 2$ (e.g., Connolly et al. 1997; Lanzetta et al. 2002; Hopkins & Beacom 2006), with a decline toward both lower (e.g., Lilly et al. 1996; Dickinson et al. 2003; Le Floc'h et al. 2005; Iglesias-Páramo et al. 2007; Wang et al. 2013) and higher redshifts (e.g., Pérez-González et al. 2005; Wall et al. 2008; Wuyts et al. 2011; Béthermin et al. 2012). Further evidence for this connection includes the $M_{\rm bh}-\sigma$ relation (e.g., Magorrian et al. 1998; Tremaine et al. 2002); the presence of luminous,

coeval starbursts and AGNs in galaxies (Farrah et al. 2003; Alexander et al. 2005; Lonsdale et al. 2006; Hernán-Caballero et al. 2009; Spoon et al. 2013); and observed scaling relations between AGN properties and star formation rates in luminous quasars (Harris et al. 2016). Finally, star formation and AGN activity may directly affect each other (Fabian 2012) via both quenching (e.g., Di Matteo et al. 2005; Bower et al. 2006; Springel et al. 2006; Farrah et al. 2012; Alatalo et al. 2015) and triggering (e.g., De Young 1989; King 2005; Croft et al. 2006; Gaibler et al. 2012; Ishibashi et al. 2013; Silk 2013; Zubovas et al. 2013).

The role of AGNs during the peak epoch of galaxy assembly at $z \sim 2$ can be studied by identifying active galaxies at high redshift, characterizing the power sources within them, and determining which mechanisms trigger these power sources. Doing so, however, faces two challenges. First, star-forming regions and AGNs are often occulted by large column densities of gas and dust. Thus, a substantial fraction of their light is observed in the infrared (Sanders & Mirabel 1996; Lagache et al. 2005; Farrah et al. 2013; Casey et al. 2014). Second, at high redshifts, obscured systems are seen both faintly and at coarsened spatial scales, making them difficult to identify.

High-redshift obscured systems can be identified via several approaches, including hard X-ray flux, rest-frame optical line ratios, and infrared photometry. In the case of infrared photometry, the selection is based on colors involving at least one infrared band, where the choice of bands predisposes the selection to sources with different effective dust temperatures. This includes sources with cold (up to about 40 K) dust heated by star formation in the case of submillimeter selection or hotter dust heated by AGNs in the case of mid-infrared color selection. In the case of selections that use one optical and one infrared band and then demand an excess in the infrared band, such as the "dust-obscured galaxy" (DOG) selection, the result is usually a mixture of AGNs and starburst-dominated systems (Dey et al. 2008).

Determining the power source of obscured systems is more challenging. In the local universe, it is possible to diagnose obscured power sources with reasonable accuracy, leading to the consensus that the majority of systems with infrared luminosities up to about $10^{12} L_\odot$ (the luminous infrared galaxies, or LIRGs) are starburst-dominated (Stierwalt et al. 2013; Petty et al. 2014). At infrared luminosities exceeding $10^{12} L_\odot$ (the ultraluminous infrared galaxies, or ULIRGs), there is a greater contribution from obscured AGNs (Genzel et al. 1998; Farrah et al. 2003). At higher redshifts, however, such diagnoses are harder. For example, submillimeter-selected galaxies (SMGs) often contain obscured luminous AGNs, despite the predilection of their selection for star formation (Alexander et al. 2005). Other selections, such as the DOG selection, require additional diagnostics that use mid-infrared continuum shapes to classify sources as starburst- or AGN-dominated.

Establishing what mechanisms trigger their infrared emission is a conceptually similar challenge. At low redshifts, it is straightforward to quantify morphologies as a route to answering this question; LIRGs have diverse morphologies, but ULIRGs are almost exclusively mergers (Surace et al. 1998; Farrah et al. 2002; Bridge et al. 2007; Haan et al. 2011). The greater diversity in LIRG morphologies may reflect the broader set of evolutionary pathways that a galaxy can take through a LIRG, rather than the more luminous ULIRG, phase (e.g., Farrah et al. 2009). Outside the local universe, however, there remains significant uncertainty. For ULIRGs, the merger fraction probably declines by at most a small amount between $z = 0$ and 1 (Hung et al. 2014), but the behavior at $z > 1$ is less clear. Some studies find that $z \gtrsim 1$ infrared-luminous systems are mostly mergers (Ricciardelli et al. 2010; Zamojski et al. 2011; Alaghband-Zadeh et al. 2012; Ivison et al. 2012; Kartaltepe et al. 2012; Chen et al. 2015; Olivares et al. 2016), while others find that they are not (Melbourne et al. 2009; Ricciardelli et al. 2010; Aguirre et al. 2013; Wiklind et al. 2014), instead resembling either early types (Swinbank et al. 2010) or disks (Targett et al. 2011; Schawinski et al. 2012; Tacconi et al. 2013; Targett et al. 2013). This disagreement is mirrored by theoretical work; some models invoke mergers (Baugh et al. 2005; Chakrabarti et al. 2008; Hopkins et al. 2010; Hayward et al. 2011), some invoke "secular" processes (Dekel & Birnboim 2006; Genel et al. 2008; Dekel et al. 2009; Kereš et al. 2009; Davé et al. 2010; Narayanan et al. 2015), and others use both (Hayward et al. 2013).

For these reasons, it is valuable to employ photometric selections that isolate different populations of high-redshift LIRGs and then use both the diagnostics of their power source and measures of their morphology to place them in the wider context of galaxy assembly. Moreover, it is valuable to study the most luminous AGNs in the universe—systems with bolometric luminosities exceeding $\sim 10^{47}$ erg s^{-1}. Although rare, such systems probe the role of AGNs in galaxy assembly at their most extreme limits and can supply stringent tests for galaxy evolution models because they imply sustained, very high accretion rates of $\gg 10 M_\odot$ yr^{-1}.

In this paper, we undertake such a study with a sample of 12 extremely infrared-luminous AGN-dominated systems at $z \sim 2$, all with spectroscopic redshifts, selected with data from the *Wide-field Infrared Survey Explorer* (*WISE*; Wright et al. 2010). We then use both multiband infrared photometry and *Hubble Space Telescope* (*HST*) imaging to elucidate their evolutionary status. We adopt Vega magnitudes and assume a spatially flat cosmology with $\Omega_m = 0.3$ and $H_0 = 70$ km s^{-1} Mpc^{-1}.

2. Sample Selection

Searches within the *WISE* color space have isolated populations ranging from planets to galaxies (Cushing et al. 2011; Griffith et al. 2011; Eisenhardt et al. 2012; Stern et al. 2012; Wu et al. 2012; Assef et al. 2013; Bridge et al. 2013; Lonsdale et al. 2015). For high-redshift an approach that has proved successful is to search for objects that are clearly detected in both the 12 μm (*W*3) and 22 μm (*W*4) channels but are weakly or not detected in the 3.4 μm (*W*1) and 4.6 μm (*W*2) channels (Eisenhardt et al. 2012; Bridge et al. 2013). The targets in this paper are selected using this approach.

The parent sample of 53 objects was selected from the AllWISE catalog (Cutri et al. 2014) and includes all objects with a spectroscopic redshift as of 2013 April. These redshifts span $1.6 < z < 4.6$. Since we are selecting those objects from the parent catalog that have redshifts, there is the possibility of bias toward higher-surface-brightness systems with bright emission lines. We do not, however, consider this bias in our analysis, as it is impossible to quantify with existing data.

The objects in the parent sample are selected in two ways. First is that of Eisenhardt et al. (2012), who demanded that sources be detected at $>5\sigma$ in both the *W*3 and *W*4 channels and have a *W*1 flux of $<34 \mu$Jy. Second is that of Bridge et al. (2013), who also demanded that sources be detected at $>5\sigma$ in both the *W*3 and *W*4 channels, a nondetection in Sloan Digital Sky Survey (SDSS) r' imaging (i.e., $r' \geqslant 22$), but then demanded only that $W2 - W3 \geqslant 4.8$. Both selections result in a source density of one per several square degrees (Assef et al. 2015). These selections lie within the DOG selection, $f_{22} > 0.3$ mJy and $f_{22}/f_R > 1000$ (Dey et al. 2008), but result in samples with higher dust temperatures, on average; the DOGs have $T_d \sim 30$–40 K (Pope et al. 2008; Melbourne et al. 2012), whereas our selections have $T_d \simeq 60$ K (Bridge et al. 2013; Jones et al. 2014). While the Eisenhardt et al. (2012) and Bridge et al. (2013) selections differ in detail, hereafter we treat them as identical and refer to them as "Hot DOGs," or *h*DOGs (Wu et al. 2012).

3. Observations

3.1. HST Observations

We submitted the 53 objects in the parent sample for a Cycle 19 *HST* Snapshot program (*HST*-GO-12585; PI: Petty), of

Table 1
The *WISE*-Selected Hot DOG Sample and Their Flux Densities from *HST*, *WISE*, and *Herschel*

Object	HST	WISE				Herschel-PACS		Herschel-SPIRE		
	1.6 μm (μJy)	3.4 μm (μJy)	4.6 μm (μJy)	12 μm (mJy)	22 μm (mJy)	70 μm (mJy)	160 μm (mJy)	250 μm (mJy)	350 μm (mJy)	500 μm (mJy)
WISEA J042138.55+203644.6	9.2 ± 0.8	11.0 ± 6.6	25.0 ± 9.7	2.7 ± 0.2	9.2 ± 1.1	30 ± 5	17 ± 18	27 ± 10	20 ± 15	17 ± 10
WISEA J051442.62−121724.4	67.9 ± 2.1	107.0 ± 5.7	124.0 ± 10.2	5.9 ± 0.2	30.1 ± 1.3	105 ± 11	165 ± 20	110 ± 12	51 ± 10	18 ± 9
WISEA J054230.90−270539.8[a]	7.8 ± 0.7	14.8 ± 3.8	30.8 ± 12.3	2.8 ± 0.1	14.7 ± 1.0	43 ± 4	63 ± 11	47 ± 6	23 ± 10	16 ± 11
WISEA J060508.95−232434.5	8.2 ± 0.7	24.3 ± 3.9	76.9 ± 8.4	3.9 ± 0.2	16.3 ± 1.0	34 ± 5	117 ± 20	103 ± 15	58 ± 10	26 ± 10
WISEA J091247.26+774158.2	13.7 ± 0.9	73.7 ± 2.8	25.3 ± 7.0	1.9 ± 0.1	8.3 ± 7.8	27 ± 6	17 ± 12	15 ± 12	11 ± 10	9 ± 15
WISEA J120629.69+623224.3	6.9 ± 0.7	18.7 ± 3.4	27.3 ± 6.7	2.3 ± 0.1	11.8 ± 0.9	37 ± 7	30 ± 13	33 ± 10	14 ± 11	16 ± 18
WISEA J131628.54+351235.6[b]	9.8 ± 0.8	16.6 ± 3.6	39.3 ± 7.7	3.3 ± 0.1	12.8 ± 1.0	27 ± 6	41 ± 4	39 ± 8	12 ± 10	11 ± 13
WISEA J171946.63+044635.4	19.8 ± 1.1	28.5 ± 4.5	109.0 ± 10.5	5.2 ± 0.2	15.2 ± 1.2	35 ± 6	43 ± 8	69 ± 6	56 ± 5	40 ± 7
WISEA J182242.67+634853.4	8.9 ± 0.8	37.2 ± 2.2	134.0 ± 5.2	3.6 ± 0.1	12.1 ± 0.6	26 ± 5	10 ± 12	9 ± 10	12 ± 10	6 ± 14
WISEA J183013.51+650420.4[c]	1.5 ± 0.3	11.4 ± 1.6	13.1 ± 3.3	2.4 ± 0.1	7.4 ± 0.5	17 ± 6	25 ± 10	14 ± 7	16 ± 9	7 ± 13
WISEA J183533.73+435548.7[d]	12.8 ± 0.9	32.0 ± 2.6	139.0 ± 6.5	6.8 ± 0.2	27.4 ± 1.0	54 ± 5	81 ± 21	113 ± 12	82 ± 9	46 ± 7
WISEA J233759.50+792654.6	21.8 ± 1.2	31.0 ± 4.0	70.3 ± 6.4	2.3 ± 0.1	14.6 ± 0.9	64 ± 7	101 ± 12	58 ± 7	38 ± 6	17 ± 10

Notes. We also include ground-based far-infrared photometry from Wu et al. (2012) and Jones et al. (2014), listed below.
[a] <47 mJy at 350 μm.
[b] <14.2 mJy at 1100 μm.
[c] <31 mJy at 350 μm.
[d] 46 ± 16 mJy at 350 μm, 31 ± 14 mJy at 450 μm, 8 ± 1.5 mJy at 850 μm.

which 12 were observed (Table 1). These 12 objects have spectroscopic redshifts in the range $1.8 < z < 2.7$. Other than a slightly lower median redshift, these 12 objects are statistically indistinguishable from the parent sample. None of their spectra show evidence for foreground lenses.

The 12 objects were observed with the Wide Field Camera 3 (WFC3) in the F160W filter (hereafter H-band). To facilitate the SNAP observations, the total exposure time per object was 1500 s, selected because it allowed each object to be observed within 48 minutes, after accounting for guide star acquisition and instrument overheads. This exposure time reaches a surface brightness limit in H of 23.5 mag arcsec^{-2}. Each exposure was divided into four equal-length subexposures using a dither box pattern of four pointings with $0\farcs6$ spacing.

All of the sample was clearly detected by WFC3. The WFC3 data were reduced using a standard Multidrizzle process. We started with the persistence-corrected output files from the *calwf3* pipeline, which performs standard tasks including bias and dark current subtraction, linearity correction, flat fielding, bad-pixel masking, and removal of cosmic rays. We then removed geometric distortion from each file and combined them into a single image for each object using the Autodrizzle task. To extract fluxes, we used SExtractor (Bertin & Arnouts 1996) in MAG_BEST mode, which first determines the most appropriate elliptical aperture to use and then measures the flux inside that aperture. Finally, we corrected the photometry for Galactic absorption and converted the fluxes into magnitudes using the zero points provided by the WFC3 team.

3.2. Ancillary Data

We obtained reduced *Spitzer* (Werner et al. 2004) images at 3.6 and 4.5 μm from the IRAC instrument (Fazio et al. 2004) for our sample. These observations are significantly deeper than the $W1$ and $W2$ observations. For photometry, we adopted the methods in Lacy et al. (2005). We required 2σ levels for the detect and analysis threshold parameters and checked each object map for false detections.

We obtained *Herschel* (Pilbratt et al. 2010) photometry for all of our sample from the *Herschel* Science Archive. The data were taken with the Photoconductor Array Camera and Spectrometer (PACS; Poglitsch et al. 2010) at 70 and 160 μm and with the Spectral and Photometric Imaging REceiver instrument (SPIRE; Griffin et al. 2010) at 250, 350, and 500 μm. The level 1 data were processed to level 2 using the *Herschel* Interactive Processing Environment (HIPE) version 14.2.0. For PACS, aperture photometry was carried out using the scanmap_pointsources_PhotProject.py HIPE script. For SPIRE, photometry was carried out using the Sussextractor algorithm (Savage & Oliver 2007; Wang et al. 2014). The complete set of *Herschel* data for the hDOGs, including those without *HST* data, is presented in C-W Tsai et al. (2017, in preparation).

4. Methods

4.1. Morphologies

We use five parameters to quantify the morphologies of our sample: Gini (G), M_{20}, asymmetry (A), Sérsic index (n), and effective radius (r_e).

The Gini coefficient (Abraham et al. 2003) is a measure of how concentrated the light is in an image:

$$G = \frac{1}{|\bar{f}|N(N-1)} \sum_{i=1}^{N} (2i - N - 1)|f_i|, \tag{1}$$

where $|\bar{f}|$ and $|f_i|$ are the absolute average flux and ith pixel flux from N total pixels, respectively. Here G ranges from zero to unity, with low values for galaxies with even light distributions and high values for galaxies whose light is concentrated into a small number of bright nuclear pixels. The M_{20} coefficient (Lotz et al. 2004) is the second-order moment of the brightest 20% of the light,

$$M_{20} = \log_{10}\left(\frac{\sum_i M_i}{M_{\text{tot}}}\right), \tag{2}$$

where

$$M_i = f_i [(x_i - x_c)^2 + (y_i - y_c)^2], \tag{3}$$

with

$$\sum_i f_i < 0.2 f_{\text{tot}}, \tag{4}$$

in which f_i is the flux at (x_i, y_i), and (x_c, y_c) is the galaxy centroid. Here M_{20} is a measure of the variance of the brightest 20% of the light and is anticorrelated with concentration; a single-nucleus system will have a more negative M_{20} value than a double-nucleus system, for example. The asymmetry, A, is a measure of the mirror, or central rotational, symmetry of all of the light from a galaxy (Abraham et al. 1994; Conselice et al. 2000). It is determined by subtracting from the original image I_0 a 180° rotated image I_ϕ:

$$A = \frac{\Sigma |I_0 - I_\phi|}{2\Sigma |I_0|}. \tag{5}$$

The Sérsic index (Sérsic 1963) is defined in the radial light intensity profile,

$$I(r) \propto e^{-\kappa\left(\frac{r}{r_e}\right)^{1/n}}, \tag{6}$$

and is also called the concentration, or curvature, index. Finally, the effective radius, r_e, is the radius that encloses half of the total light emitted by the object.

We adopt the G, M_{20}, and A statistics because they have been used in many previous studies and their values have been compared against results from numerical simulations to calibrate morphological classifications (Lotz et al. 2008b). We include the Sérsic index and effective radius because they contain information complementary to the Gini coefficient. Both n and G are measures of central concentration, but n also depends on profile shape, in that increasing n gives a brighter center and a shallower falloff at large radii. Effective radius gives an estimate of the absolute size of an object. We use a Sérsic profile to fit our sample rather than, e.g., a Nuker profile (Hernquist 1990; Lauer et al. 1995), since each object covers a small number of pixels; fitting a geometric mean is thus more meaningful than considering minor and major axes separately.

To perform the G, M_{20}, and A measurements, we followed the approaches taken in Lotz et al. (2004) and Petty et al. (2009). We first subtracted an average sky flux from each frame, computed using the IRAF task imexamine. We then

calculated the total flux within 1.5 times the Petrosian radius (r_p). Photometric uncertainties were estimated by changing the H-band center by up to $5''$ in random directions about the best-fit galaxy centroid, measuring G, M_{20}, and A using the same radius, and calculating the standard error from 1000 iterations of this step. To estimate Sérsic indices and effective radii, we used GALFIT (Peng et al. 2002) to fit two-dimensional profiles of the form in Equation (6), following the approaches of previous authors (Ravindranath et al. 2006; Petty et al. 2009).

The light profiles of two objects—W0514 and W2337—suggested that point spread function (PSF) subtraction might unveil more details of the host galaxy, but our attempts to do so were unsuccessful. When we included a PSF, generated using the Tiny Tim tool, as an additional component within GALFIT when fitting these two objects, we could not extract stable host galaxy parameters, and the fit quality did not improve. We therefore conclude that an emerging AGN in the optical is unlikely in any part of our sample, but we cannot exclude that AGN light affects the central few pixels.

4.2. Infrared Emission

To quantify the origin—AGN activity or star formation—of the infrared emission, we fit radiative transfer models to the $WISE$, PACS, and, where available, submillimeter and millimeter-wave photometry. We do not fit to data at observed-frame $4.5\,\mu m$ and shorter wavelengths due to the possibility of host galaxy contamination, but we do include these data as limits.

We assume that the infrared emission arises from a single episode of AGN activity and/or star formation. We then fit the infrared data simultaneously with two grids of precomputed radiative transfer models: one for AGNs (Efstathiou & Rowan-Robinson 1995; Efstathiou et al. 2013) and one for starbursts (Efstathiou et al. 2000). A model set for old stellar populations is not included, since it is likely that the infrared emission redward of $4.5\,\mu m$ comes predominantly from obscured luminous activity, with a negligible contribution from unobscured older stars. These models have been used previously in Verma et al. (2002), Farrah et al. (2002, 2003, 2012), and Efstathiou et al. (2013). The AGN models assume that the dust geometry is a smooth tapered disk whose height, h, increases linearly with distance, r, from the AGN until it reaches a constant value. The dust distribution includes multiple species of varying sizes and assumes that the density distribution scales as r^{-1}. The starburst models combine the population synthesis code of Bruzual & Charlot (2003) with a prescription for radiative transfer through dust that includes the effects of small dust grains and polycyclic aromatic hydrocarbons (PAHs; Efstathiou & Siebenmorgen 2009). In total, there are 1680 starburst models and 4212 AGN models.

Both model sets have several free parameters (e.g., inner half-opening angle for the AGNs, age and initial optical depths of the molecular clouds for the starbursts), which we lack the data to constrain. Instead, we use the full model sets to obtain a realistic estimate of the uncertainties on the luminosities by using all possible combinations of SED fits for each object to construct a weighted probability distribution for the total, AGN, and starburst luminosities. The only constraint we impose is on the AGN model set: that the viewing angle is greater than the torus half-opening angle, as measured from pole-on, so that the broad-line region is not visible in direct light. This reduces the number of AGN models to 2064. This approach assumes that all models exist in the high-redshift population and are comparably likely. This assumption lacks strong supporting evidence, but the model sets do span the properties found in lower-redshift populations. Moreover, our approach is superior to simply normalizing a single template or fitting a small number of templates, as such an approach is effectively a small set of δ functions in the same parameter space.

5. Results and Analysis

The HST images are presented in Figure 1. We do not present the $WISE$ and $Herschel$ images, as they are in all cases consistent with point sources; see Section 5.2. The H-band, $WISE$, PACS, and SPIRE fluxes are presented in Table 1. The morphological parameters and infrared luminosities are presented in Table 2. The infrared SEDs are presented in Figure 2.

5.1. Comparison Samples

In the following, we make comparisons to five samples from the literature. First are the "bump" DOGs (bDOGs) and "power-law" DOGs (pDOGs; Bussmann et al. 2009, 2011; Melbourne et al. 2012). The bDOGs have mid-infrared continua showing an opacity minimum arising from H^- in stellar atmospheres, while the pDOGs have mid-infrared continua showing an AGN power law. The bDOGs have fainter $22\,\mu m$ flux densities and less extreme $R - [22]$ colors than the pDOGs. Second are two samples of SMGs, one from Bussmann et al. (2011) and one from Aguirre et al. (2013). The SMGs from Bussmann et al. (2011) are the 25 SMGs with redshifts in the range $0.7 < z < 3.4$, originally presented in Swinbank et al. (2010) and selected from the spectroscopic catalog of Chapman et al. (2005). The parent sample is the radio-identified subset of sources detected at $850\,\mu m$ in surveys with the Sub-millimeter Common User Bolometer Array (SCUBA). The SMGs from Aguirre et al. (2013) lie in approximately the same redshift range as our sample and include both unlensed and lensed sources and sources selected at both $850\,\mu m$ and $1.2\,mm$. While their selection is heterogeneous compared to that of Bussmann et al. (2011), they publish asymmetries, so we include them for comparison. The final comparison sample is the sample of $M_* > 10^{11}\,M_\odot$ galaxies at $1.7 < z < 3.0$ from the GOODS NICMOS Survey (GNS; Buitrago et al. 2008; Conselice et al. 2011). This sample comprises massive galaxies with infrared luminosities much lower than any of the other comparison samples and is not subdivided into quiescent and star-forming subsamples.

Each comparison sample includes only a subset of the morphological parameters we consider. In summary, the samples used for morphological comparisons are:

1. hDOGs (#1, our sample): G, M_{20}, A, r_e, and n
2. bDOGs (#2, Bussmann et al. 2011): G, M_{20}, r_e, and n
3. pDOGs (#3, Bussmann et al. 2009): G, M_{20}, r_e, and n
4. B12 SMGs (#4, Bussmann et al. 2011): G, M_{20}, r_e, and n
5. A13 SMGs (#5, Aguirre et al. 2013): G, M_{20}, and A
6. GNS galaxies (#6, Buitrago et al. 2008): G, M_{20}, A, r_e, and n

All of the comparison samples were observed by HST at rest-frame wavelengths closely matched to our sample (we do not consider the minor difference in resolution between
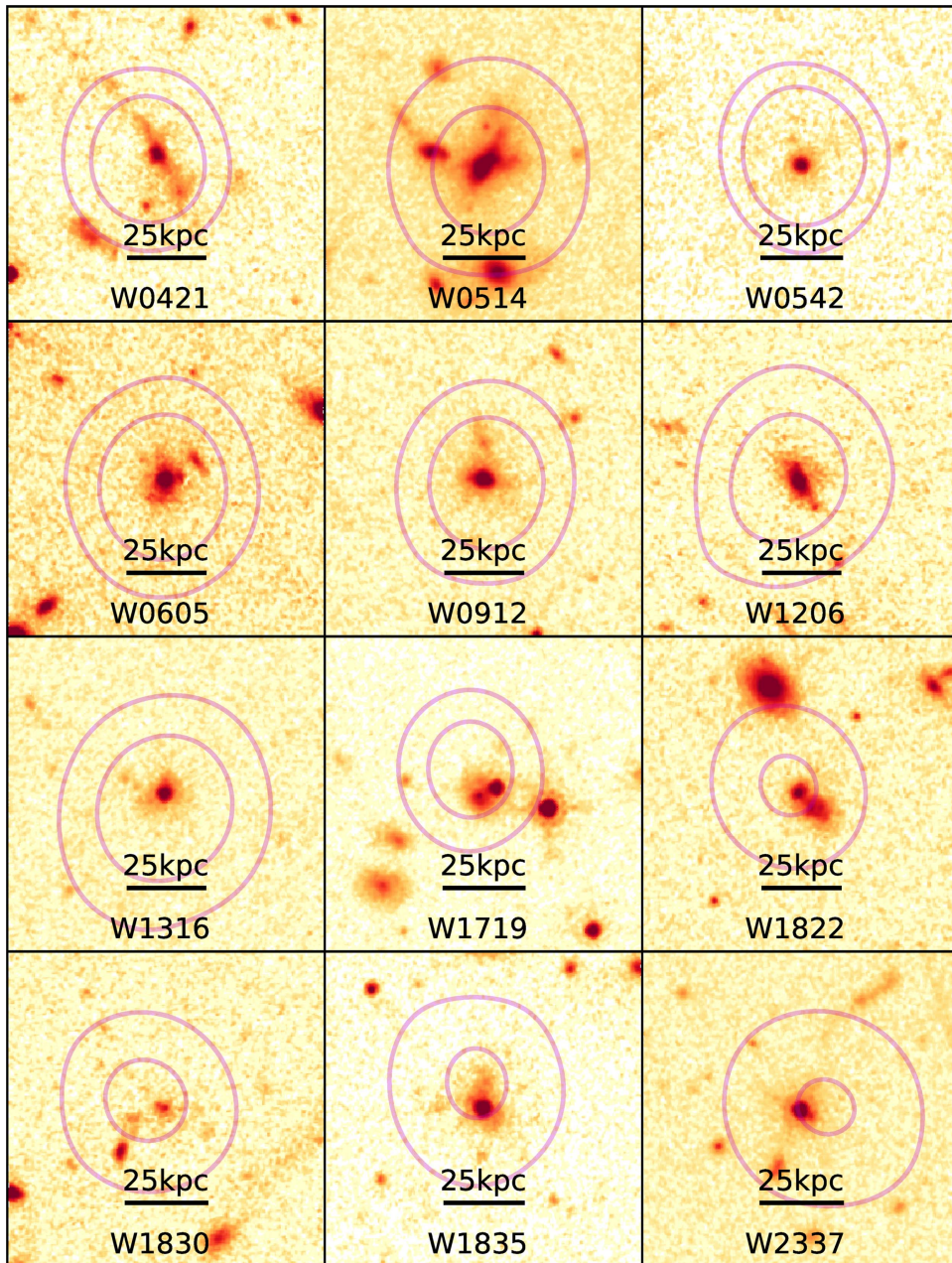
Figure 1. The *H*-band morphologies of the 12 objects in our sample. For each object, the panel shows the WFC3 image with the *W*3 contours overlaid. We do not show the *WISE*, PACS, or SPIRE images, as the detections are always point sources that are well centered on the *HST* sources.

NICMOS-NIC2 and redrizzled WFC3). In all cases, we include only those objects within approximately the same redshift range as our sample. At $z = 2$, the spatial scale is $8.37 \, \mathrm{kpc \, arcsec^{-1}}$. For these reasons, we do not include comparisons to objects within the COSMOS field observed with the Advanced Camera for Surveys (ACS) or to low-redshift ULIRGs and Hubble sequence galaxies (Lotz et al. 2004), as the finer spatial resolution and different rest-frame wavelengths could lead to invalid comparisons.

To make quantitative comparisons between populations, we employ two-sample Bayesian hypothesis testing using a nonparametric Polya tree prior (Holmes et al. 2015). This approach is superior to the traditional Kolmogorov–Smirnov test (or other frequentist approaches), as it gives the probability *for* the null hypothesis that the two populations are identical, rather than the probability of obtaining the same or a more extreme result *assuming* that the two populations are identical. The probabilities are given in Table 3.

5.2. Infrared Luminosities and Colors

In the *WISE* images, our sample is consistent with point sources at 12 and 22 μm. The PACS and SPIRE images are also consistent with point sources. In all cases, the *WISE* and (where detected) *Herschel* sources are centered closely on the primary *HST* source. This, combined with the absence of foreground objects in the spectra and the *h*DOG selection that biases against bright foreground objects, means that significant gravitational-lensing amplification of our sample is unlikely.

The fitted total rest-frame infrared luminosities of our sample span 1.8×10^{13} to $1.4 \times 10^{14} \, L_\odot$, making them among the

Table 2
Redshifts, Luminosities, and Morphological Parameters

Object	z	L_{IR} $(10^{13} L_\odot)$	f_{AGN}	G	M_{20}	A	n	r_e (kpc)
WISEA 0421	1.83	2.09 ± 0.18	$1.00^{+u}_{-0.13}$	0.575 ± 0.031	-1.822 ± 0.146	0.26 ± 0.03	1.20	3.34
WISEA 0514	2.50	14.2 ± 1.00	$0.91^{+0.04}_{-0.04}$	0.811 ± 0.045	-2.260 ± 0.203	0.39 ± 0.07	0.70	2.54
WISEA 0542	2.53	6.77 ± 0.50	$0.90^{+0.02}_{-0.03}$	0.775 ± 0.037	-1.520 ± 0.205	0.33 ± 0.04	1.01	1.38
WISEA 0605	2.08	4.78 ± 0.25	$0.69^{+0.06}_{-0.05}$	0.674 ± 0.035	-2.278 ± 0.202	0.16 ± 0.02	2.01	3.36
WISEA 0912	2.00	1.87 ± 0.30	$0.95^{+0.05}_{-0.10}$	0.745 ± 0.046	-2.102 ± 0.362	0.18 ± 0.03	1.27	2.43
WISEA 1206	2.00	2.57 ± 0.50	$1.00^{+u}_{-0.25}$	0.628 ± 0.027	-2.460 ± 0.258	0.17 ± 0.03	2.12	5.40
WISEA 1316	1.96	3.03 ± 0.30	$0.83^{+0.10}_{-0.10}$	0.784 ± 0.045	-1.941 ± 0.351	0.24 ± 0.04	1.50	1.72
WISEA 1719	2.54	8.76 ± 0.90	$0.99^{+0.01}_{-0.02}$	0.804 ± 0.043	-2.044 ± 0.183	0.74 ± 0.13	1.32	4.03
WISEA 1822	2.07	3.30 ± 0.30	$0.98^{+0.02}_{-0.07}$	0.663 ± 0.037	-2.073 ± 0.177	0.29 ± 0.05	0.29	6.21
WISEA 1830	2.65	4.41 ± 0.35	$0.96^{+0.04}_{-0.03}$	0.525 ± 0.025	-0.878 ± 0.119	0.24 ± 0.04	1.18	2.80
WISEA 1835	2.30	9.62 ± 0.50	$0.83^{+0.07}_{-0.10}$	0.472 ± 0.026	-1.362 ± 0.114	0.22 ± 0.03	1.33	1.81
WISEA 2337	2.74	10.1 ± 1.00	$0.90^{+0.08}_{-0.15}$	0.826 ± 0.034	-1.808 ± 0.107	0.37 ± 0.05	1.34	1.18

Notes. The methods used to compute these quantities are described in Section 4. The uncertainties on the effective radii and Sérsic indices are approximately 15% in all cases.

most luminous objects in the universe (see also Bridge et al. 2013; Tsai et al. 2015). They are much more infrared-luminous than $z < 0.2$ ULIRGs (e.g., Farrah et al. 2003) and have comparable luminosities to hyperluminous infrared galaxies (HyLIRGS) found at other redshifts that were selected at observed-frame wavelengths of less than 100 μm (Rowan-Robinson 2000). They match or exceed the luminosities found for the most luminous SMGs (Chapman et al. 2005). Four members of our sample (W0542, W1316, W1830, and W1835) have infrared luminosities in Fan et al. (2016); in three cases, our luminosities are consistent with theirs, while for the fourth (W1835), our luminosity is a factor of 2 higher. This difference likely arises from our more comprehensive infrared data and the different approaches to modeling the AGN and starburst emission. W1835 also has a published infrared luminosity in two previous papers; our luminosity is 60% higher than that derived by Wu et al. (2012) but consistent with the (template) luminosity of Jones et al. (2014).

The combination of *WISE*, PACS, SPIRE, and (in some cases) ground-based submillimeter and millimeter-wave photometry means we can constrain the fraction of the total infrared luminosity that arises from AGNs (f_{AGN}). In all cases, the infrared SED fits mark our sample as consisting of luminous, obscured, AGN-dominated systems. In some cases, it is possible to explain all of the infrared emission as arising from AGN activity, though the best-fit solution usually includes some star formation, with star formation rates of up to a few hundred $M_\odot$ yr^{-1}. The AGN fractions of our sample are consistently higher than those in the *b*DOGs and higher or comparable to those in the *p*DOGs (Pope et al. 2008; Assef et al. 2015).

We note three caveats to the results from the infrared SEDs. First, since the AGN models are axisymmetric, the total infrared luminosity cannot be precisely inferred simply by integrating the line-of-sight infrared luminosity over 4π sr. However, in all cases, the anisotropy correction to the AGN luminosity is a factor of 2 or less, and, in most cases, the 1σ uncertainties on the anisotropy correction encompass unity, so we do not apply them here. Second, there is a possibility that the bias toward hotter dust in our sample compared to other classes of DOGs is consistent with younger starbursts, rather than a particular AGN phase. This possibility arises

because younger starbursts have a more intense interstellar radiation field and therefore have elevated dust temperatures compared to older starbursts (Efstathiou & Siebenmorgen 2009). We cannot, however, explore this possibility, since the lack of rest-frame mid-infrared spectra means that the constraints on the starburst ages from the model fits are weak —the 90% confidence intervals on the starburst ages are 10–60 Myr or wider in all cases. Tighter constraints than this would require higher-quality infrared data (Farrah et al. 2016). Third, we cannot exclude the possibility of a contribution to the total infrared luminosity from "cirrus" dust heated by quiescent starlight.

Since the uncertainties on the fractional AGN luminosities are significant, we define two classes of AGN fractions for subsequent analysis. These classes are $f_{\mathrm{AGN}} < 0.95$ and $f_{\mathrm{AGN}} > 0.95$. The choice of boundary is to some extent arbitrary and is intended to help frame the discussion; we do not adopt it out of any physical motivation. We define the classes such that one is an "AGN composite" class and the other is a "pure AGN" (or close to) class.

In Figure 3, we plot the luminosities of our sample against both redshift and AGN fractional luminosity. There is, perhaps, a trend with redshift, with the more luminous objects lying at higher redshifts, though this could be a selection effect. There is also a hint of a trend with AGN fraction, with 5/6 objects with the lowest infrared luminosities having the highest AGN fractional luminosities. Compared to samples from the literature, our sample is more luminous than either the *b*DOGs or *p*DOGs by factors of approximately 3 and 10, respectively. This is consistent with the idea that the *h*DOG selection preferentially finds obscured, extremely infrared-luminous AGNs. Our sample is also more luminous than any of the SMGs in the same redshift range. Finally, we compare to the HyLIRG sample of Tsai et al. (2015; hereafter TS15). The TS15 sample was selected in the same way as ours but comprises the most luminous 20 objects in the parent spectroscopic catalog of *h*DOGs. Compared to the TS15 sample, our sample is at lower redshifts than the TS15 sample and slightly lower, on average, infrared luminosities, though at $z \gtrsim 2.2$ their luminosities are comparable.

Turning to the infrared colors, in Figure 4, we consider two color–color plots: $f_{22}/f_{12} - f_{12}/f_{1.6}$ and $f_{22}/f_{4.5} - f_{4.5}/f_{1.6}$
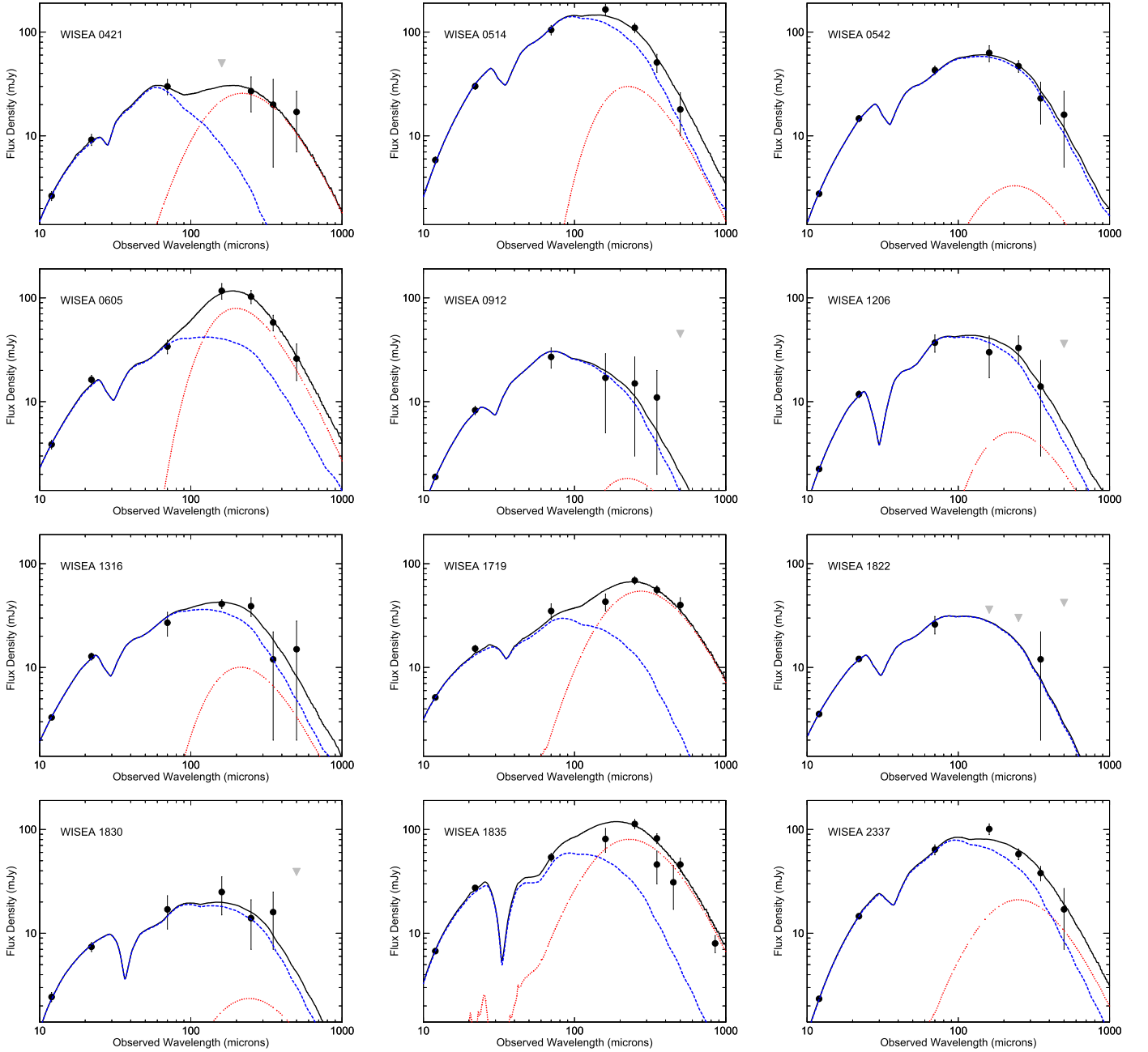
Figure 2. Mid- to far-infrared observed-frame SEDs of our sample. In each panel, the black line is the combined best-fit model, the blue dashed line is the AGN component, and the red dotted line is the starburst component. Photometry is presented as 3σ upper limits (gray triangles) if detections are below 1σ significance. The ground-based photometry from Table 1 is also plotted. We show only the SEDs at $>4.5\,\mu$m, as our fitting approach does not include a host galaxy component. Nevertheless, the fit is always consistent with the shorter-wavelength data, either as fluxes or upper limits.

(the TS15 HyLIRG sample is not plotted, because $1.6\,\mu$m photometry is not available for this sample). Starting with the $f_{22}/f_{12}-f_{12}/f_{1.6}$ plot, our sample has $f_{12}/f_{1.6}$ colors similar to those of the pDOGs, consistent with both populations having similar AGN–to–host galaxy luminosity ratios, at least at $12\,\mu$m. However, our sample has significantly redder f_{22}/f_{12} colors than the pDOGs or bDOGs. This is consistent with the AGNs in the hDOGs being more obscured than in other classes of DOG. In the $f_{22}/f_{4.5}-f_{4.5}/f_{1.6}$ plot, we see a clear separation; the hDOGs have higher $f_{22}/f_{4.5}$ ratios than the pDOGs, which are themselves higher than the bDOGs, consistent with a rising contribution from an obscured AGN for the same host galaxy mass. However, the hDOGs have lower $f_{4.5}/f_{1.6}$ ratios than

either the pDOGs or bDOGs, which are similar to each other. This is consistent with a host galaxy that is younger, less massive, and/or less obscured, and/or that there is some contribution to the optical light from the central AGN.

5.3. Morphologies

The WFC3 images show a range of morphologies. One object, W0542, has a symmetric light profile, appears undisturbed, and has no close companions. Three objects (W1206, W1316, and W1835) show evidence for a disturbed, irregular light profile but do not clearly have close companions. The remaining eight objects all show disturbed profiles with what appears to be one or more close companions. In all cases,

Table 3
Probabilities of Similarities between Our Sample and the Comparison Samples

Sample	G	M_{20}	A	r_e	n
#2: bDOGs	0.57	0.23	…	96	35
#3: pDOGs	<0.1	9.7	…	79	19
#4: B12 SMGs	1.1	2.4	…	99	99
#5: A13 SMGs	66	55	35	…	…
#6: GNS galaxies	0.12	2.2	99	82	99

Notes. The percentage probabilities that the hDOGs have a similar distribution to those of literature samples in each morphological parameter. The probabilities are computed using the approach described in Section 5.1. In the text, these probabilities are denoted $P_{1,x}^y$, where x is the population being compared against the hDOGs and y is the morphological parameter in question.

the spatial extents of the sources lie approximately in the range 10–25 kpc. No object shows evidence for significant gravitational lensing (see also Wu et al. 2014).

For an initial morphological classification, we use boundaries in the $G{-}M_{20}{-}A$ plane. In the $G{-}M_{20}$ plane, we use the boundaries determined by Lotz et al. (2008a) for mergers,

$$G > -0.14M_{20} + 0.33 \tag{7}$$

early-type systems,

$$G \leqslant -0.14M_{20} + 0.33; \ \text{and} \ G > 0.14M_{20} + 0.80 \tag{8}$$

and late-type systems,

$$G \leqslant -0.14M_{20} + 0.33; \ \text{and} \ G \leqslant 0.14M_{20} + 0.80, \tag{9}$$

as determined from comparisons to galaxies at $z \sim 0.3$ observed in the rest-frame B-band at an effective resolution of 0.62 kpc (see also Lotz et al. 2004, 2008b). To classify mergers versus nonmergers in the $G{-}A$ plane, Conselice et al. (2003) and Lotz et al. (2004) proposed a boundary of

$$G > -0.4A + 0.68; \ \text{or} \ A \geqslant 0.35. \tag{10}$$

Our sample and these boundaries are shown in Figure 5.

The use of these boundaries for our sample comes with four caveats. First, the spatial resolution at which the boundaries were determined, ∼0.6 kpc, is finer than the 1.26 kpc resolution of WFC3/IR at $z = 2$. The general effect of this is to lower the G and elevate the M_{20} values. We do not believe that this difference in resolution will impact our results, since Lotz et al. (2008a) used these boundaries up to $z = 1.2$ with little change in their effectiveness, and the change in spatial resolution from $z = 1.2$ to 2 is insignificant. Second, the boundaries were determined at a rest-frame central wavelength of ∼400 nm, compared to the ∼530 nm of our sample. The effect of this difference is that our images may be smoother, as they are less affected by extinction and do not sample any emission below the Balmer break. Quantifying the effect of this difference is beyond the scope of this paper, so we simply note it as a caveat. Third, we are assuming that the observed-frame 1.6 μm light traces stellar mass, rather than line-emitting gas, in most pixels. Based on previous observations, this seems likely (e.g., Förster Schreiber et al. 2011), but we cannot exclude the possibility of significant [O III] 5007 Å contamination. Fourth, the selection of objects with spectroscopic redshifts may predispose the sample to having more centrally concentrated rest-frame ultraviolet emission (Section 2).

Compared to the GNS sample, our sample has markedly different G values; we find that $P_{1,6}^G = 0.12\%$, with the hDOGs

having values higher by $\Delta G \sim 0.17$, on average, indicative of more centrally concentrated light distributions. The M_{20} values of our sample are also different from those of the GNS sample; we find that $P_{1,6}^{M_{20}} = 2.2\%$, with the values lower in our sample by $\Delta M_{20} \sim 0.35$, indicating that the brightest 20% of light in our sample shows less variance and is more concentrated into a small number of nuclei. Conversely, the asymmetries of the hDOGs are similar to those of the GNS sample, with $P_{1,6}^A = 99.5\%$.

Other studies similar to the GNS exist; while these studies do not tabulate their data, we can still make comparisons. Compared to the $M_* \gtrsim 10^{10} M_\odot$ systems at $z \lesssim 2$ in Lee et al. (2013), our sample has comparable G but slightly more negative M_{20} values than their quiescent samples but higher G and more negative M_{20} values than their star-forming samples. Compared to the $M_* \gtrsim 10^{11} M_\odot$ systems at $z \sim 2$ selected via extremely red "IRAC-selected Extremely Red Objects" (IERO) colors ($[z_{850}] - [3.6] > 3.25$ and $[3.6] < 21.5$; Wang et al. 2012), our sample has comparable G and slightly more negative M_{20} values than their quiescent sample but higher G and substantially more negative M_{20} values than their star-forming sample.

Comparisons to the pDOGs and bDOGs can only be made in the first panel of Figure 5, as these two samples do not have asymmetry measures. Both the pDOGs and the bDOGs separate from the hDOGs in the $G{-}M_{20}$ plane, with lower G values and less negative M_{20} values, though the pDOGs are closer to our sample in M_{20} than the bDOGs. We find, for the comparison with the bDOGs, $P_{1,2}^G = 0.56\%$ and $P_{1,2}^{M20} = 0.23\%$, while for the pDOGs we find $P_{1,3}^G = 0.07\%$ and $P_{1,3}^{M20} = 9.7\%$. Overall, the hDOGs have more concentrated and less asymmetric inner light distributions than do either other class of DOG.

Finally, we compare our sample to the two SMG samples. The distribution of the A13 SMGs is wider than that of our sample in all three panels of Figure 5; our sample lies only within part of the SMG distribution, corresponding to lower-than-average asymmetries. Conversely, the G and M_{20} values for the two samples are (marginally) comparable. We find $P_{1,5}^G = 66.4\%$, $P_{1,5}^{M_{20}} = 54.9\%$, and $P_{1,5}^A = 35.1\%$. We see no dependence on AGN fraction for members of our sample in terms of their positions within the A13 SMG distribution. Conversely, the B12 SMGs are offset from our sample and lie close to the other two DOG samples. We find $P_{1,4}^G = 1.1\%$ and $P_{1,4}^{M_{20}} = 2.4\%$. Both SMG samples also avoid the bulk of the GNS sample in all three panels.

We next examine the relations between morphological parameters and redshift (Figure 6). No trends are apparent in any parameter.[14] There are also no clear trends with AGN fraction. Finally, there are no clear trends among any of the comparison populations. This is consistent with the h/b/pDOG and SMG selections isolating brief phases in luminous galaxy evolution and with the physical processes that these selections signpost not changing substantially over $1.8 < z < 2.7$.

Next, we search for trends of morphological parameters with infrared luminosity (Figure 7). No trends are evident in any parameter. We also see no trends in any of the comparison populations. There is, perhaps, a trend between L_{IR} and G if our

---

[14] We do not consider the effects of surface brightness dimming with redshift here; our sample spans $\Delta z = 0.91$, so such effects are likely to be small in comparison with other sources of error.
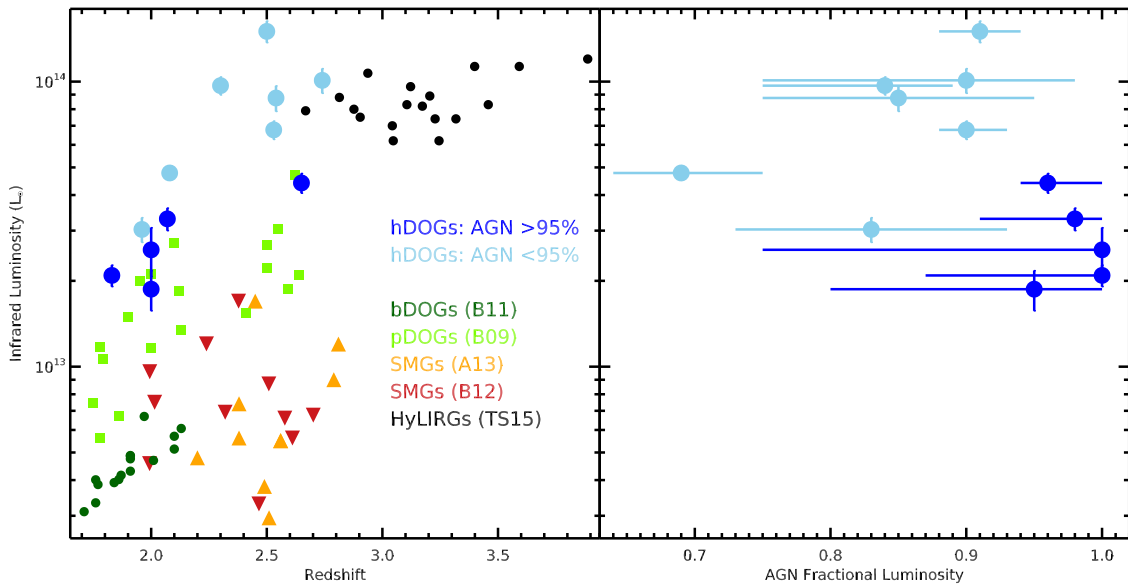
Figure 3. Infrared luminosities of the hDOGs as functions of redshift (left) and AGN fractional luminosity (right). The left panel also includes comparison populations from the literature (Section 5.1 and Tsai et al. 2015).

sample and the pDOGs are considered together, but the trend is not strong. Finally, we see no trends of morphological parameters with AGN fractional luminosity, except, perhaps, with asymmetry, where all the objects with $f_{AGN} > 0.95$ have $A < 0.35$. As with the lack of trends with redshift, this is consistent with the DOG and SMG selections isolating brief phases in the duty cycle of active galaxies and/or that infrared luminosity trends do not trace galaxy assembly processes.

5.4. Sérsic Profiles and Effective Radii

Most of our sample has Sérsic indices close to unity. Two objects have $n \sim 2$, and one has $n < 0.5$. This is at the lower end of the range of Sérsics of all galaxies, consistent with them being disk or merger systems. They are not ellipticals or systems with de Vaucoleurs profiles. Smaller, lower-luminosity ellipticals can have $n < 4$, with values as low as unity (Caon et al. 1993), but our sample members are unlikely to be small ellipticals with low Sérsic indices, given that their effective radii are all >1.15 kpc. One classification scheme that uses the Sérsic index is that of Ravindranath et al. (2006), who proposed that mergers have $\langle n \rangle < 0.8$, exponential profile systems have $0.8 < \langle n \rangle < 2.5$, and bulge systems have $\langle n \rangle > 2.5$. According to this scheme, three of our objects are mergers, while the rest are disklike.

Figure 8 compares the G, M_{20}, A, and r_e measurements for our sample to their Sérsic indices. We see no trends, except that the two objects with $n \simeq 2$ have the most negative M_{20} and lowest asymmetries, consistent with these two objects being the most dynamically relaxed of the sample. We also see no trends in Sérsic index with AGN fraction. Compared to the other samples, ours has Sérsic indices that are somewhat dissimilar to those of the two DOG samples ($P_{1,2}^n = 35.4\%$ and $P_{1,3}^n = 18.7\%$; see also Schawinski et al. 2012) but are similar to those of both the GNS sample ($P_{1,6}^n = 99.8\%$) and the B12 SMGs ($P_{1,4}^n = 99.7\%$). Compared to the Lee et al. (2013) sample, the hDOGs have Sérsic indices that are comparable to those of their star-forming $M_* \gtrsim 10^{10} M_\odot$ systems but lower by $\Delta n \simeq 1$ than those of their passive systems. The hDOG

Sérsic indices are also comparable to those of "main-sequence" star-forming galaxies (with star formation rates in the range 20–$350\, M_\odot\, yr^{-1}$) at $z \sim 2$ (the H-band single-component fits of Tacchella et al. 2015; see also Morishita et al. 2014). This similarity indirectly suggests that the star formation in hDOGs can be located at kpc-scale galactocentric distances.

Using rest-frame optical spectroscopy, Wu et al. (2017) proposed that hDOGs have black hole masses of order $10^9 M_\odot$ and Eddington ratios close to unity. We compare these measurements to the black hole masses that are predicted for our sample based on locally observed relations between n and black hole mass. These relations arise because local samples are dynamically relaxed, with a stable bulge. This condition is not satisfied in our sample. Nevertheless, we explore its consequences. Applying the log-normal relation of Graham & Driver (2007) yields predicted black hole masses for our sample of order $10^7 M_\odot$, or two orders of magnitude below the measured average. This is consistent with the idea that the black holes assembled at least a few hundred Myr before the bulges in these systems.

We compare the effective radii of our sample to the G–M_{20}–A parameters in Figure 9. No trends are apparent. The effective radii of our sample are comparable in distribution to those of all four of the comparison populations (column 5 of Table 3). They are also comparable to those of other samples of massive, star-forming galaxies at similar redshifts (Morishita et al. 2014; Tacchella et al. 2015) and larger than those of the compact star-forming or quiescent systems at $z \lesssim 2$ (Daddi et al. 2005; van Dokkum et al. 2008, 2010; Weinzirl et al. 2011). The effective radii of our sample are also similar to those of cluster galaxies at $z = 1.62$ but have lower Sérsic indices, on average (Papovich et al. 2012).

6. Discussion

The luminosities, colors, power sources, and morphologies of our sample are consistent with hDOGs signposting a brief but important stage in supermassive black hole mass assembly, during the peak epoch of galaxy assembly (Bell et al. 2012;
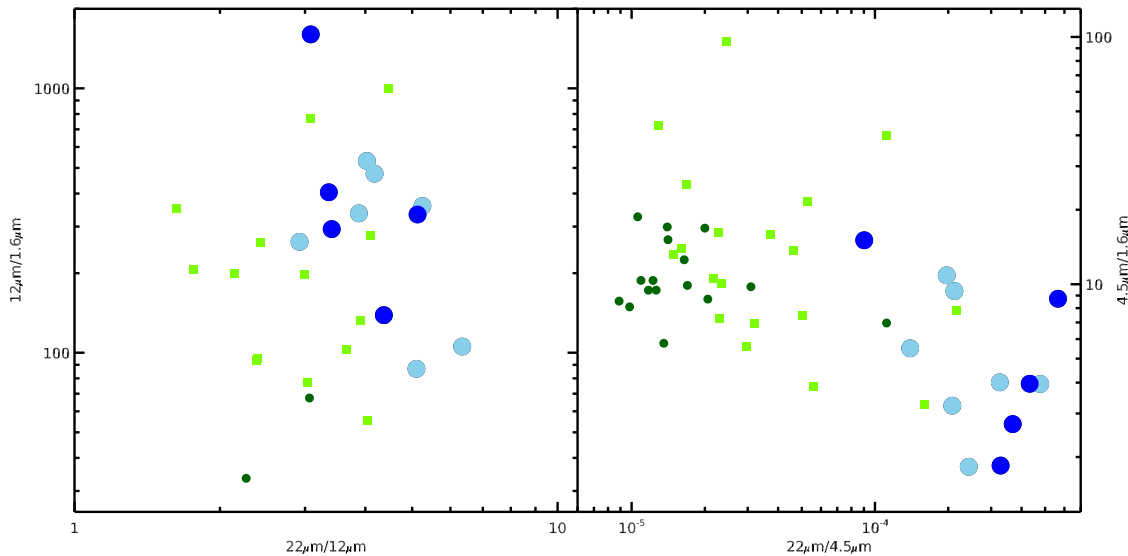
Figure 4. Two color–color plots for our sample, with the *p*DOGs and *b*DOGs (Section 5.1) also shown. Only those objects with detections in all relevant bands are plotted. See Figure 3 for a key to the points.

Andreon 2013; Bruce et al. 2014b; Morishita et al. 2015). We cannot constrain the stellar masses of our sample, so in the following we assume a stellar mass range of $10^{10-11} M_\odot$ (Assef et al. 2015). We also note two caveats. First is in the comparisons to the morphological measurements from the literature. While we have matched the samples as closely as possible in redshift and (morphological) rest-frame wavelength, there remain differences in the approach to the measurements, such as the treatment of uncertainties, that could introduce systematics between the comparison samples. Second, all the comparison samples have lower infrared luminosities than the *h*DOGs, so luminosity-driven differences are possible.

We frame the following discussion in terms of three candidate evolutionary scenarios for *h*DOGs.

1. First, *h*DOGs are predominantly major ($\lesssim$4:1) mergers, and they are "exceptional" examples of such systems— e.g., mergers with atypical progenitor properties or caught in a particular phase, such as late-stage mergers in which star formation is fading.
2. Second, *h*DOGs are predominantly mergers but are drawn at random from the merger population at $z \sim 2$.
3. Third, *h*DOGs are not preferentially associated with mergers and are instead drawn from a broad subset of the massive galaxy population at $z \gtrsim 2$.

The primary evidence that *h*DOGs are predominantly mergers is their position in the $G-M_{20}-A$ plane (Figure 5) using canonical morphological classification boundaries (Conselice et al. 2003; Lotz et al. 2004, 2008a, 2008b). In the $G-M_{20}$ plane, nine sources are classified as mergers, one as early-type, one as late-type, and one as ambiguous between all three types. In the $G-A$ plane, two sources are classified as nonmergers (the early- and late-type sources from the $G-M_{20}$ plane) while the rest are either mergers or close to the merger boundary. This is consistent with a higher merger fraction than in the massive galaxy population at $z \sim 2$. Moreover, our sample has more peaked and symmetric central light distributions than the *b*DOGs, *p*DOGs, or (most of the) SMGs, which is consistent with the *h*DOGs being more advanced mergers, on average, than any of the *b*DOGs,

*p*DOGs, and SMGs. The hint of an anticorrelation between infrared luminosity and AGN fractional luminosity (Figure 3) could also support this idea, if the peak starburst luminosity occurs before the peak AGN luminosity during a merger. Additional evidence includes the following: (1) other infrared-luminous samples often have high merger fractions at both low (Petty et al. 2014; Psychogyios et al. 2016) and high (Farrah et al. 2002; Kartaltepe et al. 2012) redshift, with late-stage mergers showing higher obscuration levels than early-stage mergers (e.g., Ricci et al. 2017); (2) reddened quasars at $z \sim 2$, which may be the immediate descendants of the *h*DOGs, have merging hosts in nearly all cases (Urrutia et al. 2008; Glikman et al. 2015; Hilbert et al. 2016); (3) an increased fraction of disturbed or interacting morphologies with increased obscuration has been found for AGNs at $z \sim 1$ (Kocevski et al. 2015); and (4) some simulations suggest that major mergers are the main mechanism for bulge growth at high redshift (Fiacconi et al. 2015).

Overall, this implies that *h*DOGs are predominantly "exceptional" late-stage mergers and that they may be (1) the descendants of some fraction of the (merger-driven) SMGs at $z \sim 2.5$ and (2) the antecedents of some fraction of both red quasars at $z \lesssim 2$ and evolved massive galaxies at $z < 2$. This scenario is consistent with that posited by Fan et al. (2016) for an overlapping but distinct sample. The rarity of *h*DOGs compared to SMGs and luminous unobscured quasars then implies that *h*DOGs are intrinsically rare—perhaps late-stage mergers with anomalously high initial gas fractions or gas-rich Mpc-scale environments—and/or that the *h*DOG phase is brief compared to the SMG and unobscured quasar phases.

We do not, however, consider this explanation satisfactory, for four reasons.

First, the evidence that *h*DOGs are predominantly mergers is less convincing when the asymmetries, effective radii, and Sérsic indices are considered individually. The *h*DOGs have identical total asymmetries to the GNS sample but dissimilar asymmetries to the SMGs. Moreover, the effective radii and Sérsic indices of the *h*DOGs are much closer in distribution to those of the GNS galaxies than those of the other three comparison samples. This is consistent with the galaxy-wide
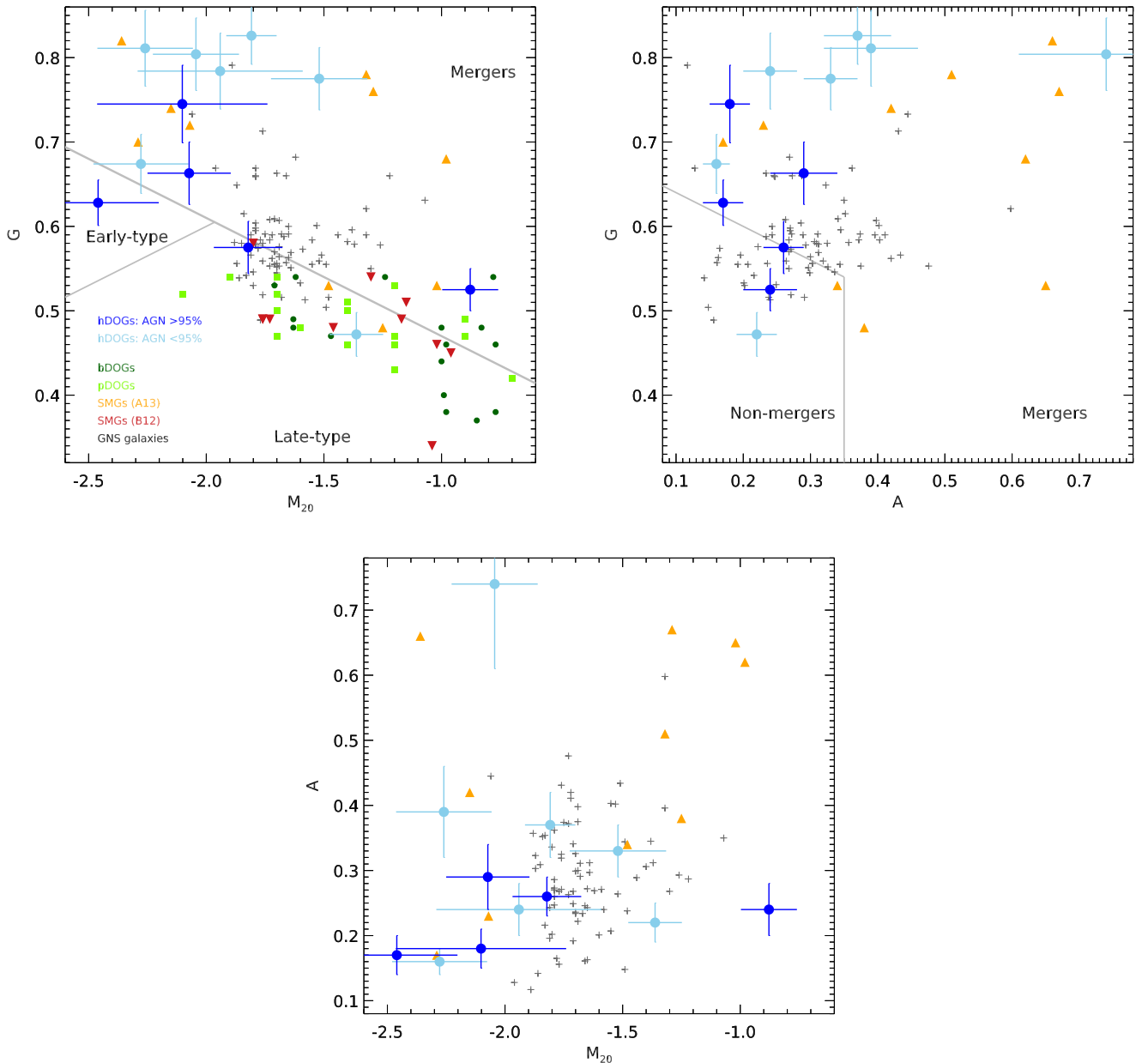
Figure 5. Locations of our sample in the G–M_{20}–A planes, including comparison populations (Section 5.1) and morphological boundaries (Section 5.3). As described in Section 4.1, G is a measure of how concentrated the light is in an image (with higher G corresponding to more concentrated light), M_{20} is a measure of the variance of the brightest 20% of the light (with more negative M_{20} corresponding to less variance), and A is a measure of the mirror symmetry of all the light from a galaxy (with higher A corresponding to greater asymmetry).

gravitational potentials of the hDOGs most closely resembling those of the GNS sample. Furthermore, if the hDOGs are late-stage mergers, then we might expect to see elliptical profiles in those systems with relaxed profiles, since massive quenched galaxies are mainly bulge-dominated at $z \lesssim 2$ (Bell et al. 2012; Wuyts et al. 2012; Bruce et al. 2014b; Lang et al. 2014; Mancini et al. 2015; Huertas-Company et al. 2016). However, we do not observe the $\langle n \rangle \gtrsim 4$ Sérsic indices of bulges in any member of our sample. Finally, in all panels of Figures 5, 8, and 9 the hDOGs appear uniquely distributed—while they may resemble other populations we consider in a single morphological parameter, they are dissimilar to all of them in any combination of morphological parameters.

Second, the infrared luminosities, AGN fractional luminosities, and effective radii of our sample show no trends with any morphological parameter. This argues against any morphological parameter coherently tracing an advancing merger.[15] We also see no trends in Sérsic index with any other parameter, arguing against mergers driving the formation of bulges.

Third, the use of the G–M_{20} plane to classify mergers at high redshift is problematic. High-redshift galaxies that contain luminous, off-center "clumps" can resemble interacting systems in G–M_{20} space, even though they are not interacting (e.g., Förster Schreiber et al. 2006; Thompson et al. 2015).

Fourth, recent simulations propose that asymmetry alone is a better discriminant of major mergers than G or M_{20}, and that objects with $A > 0.8$ are mergers, rather than the canonical

---

[15] One way to alleviate this argument is that hDOGs are a brief phase in the lifetime of a merger and are triggered at random points in the merger, so as to obtain the wide spread in G, M_{20}, and A values that we see.
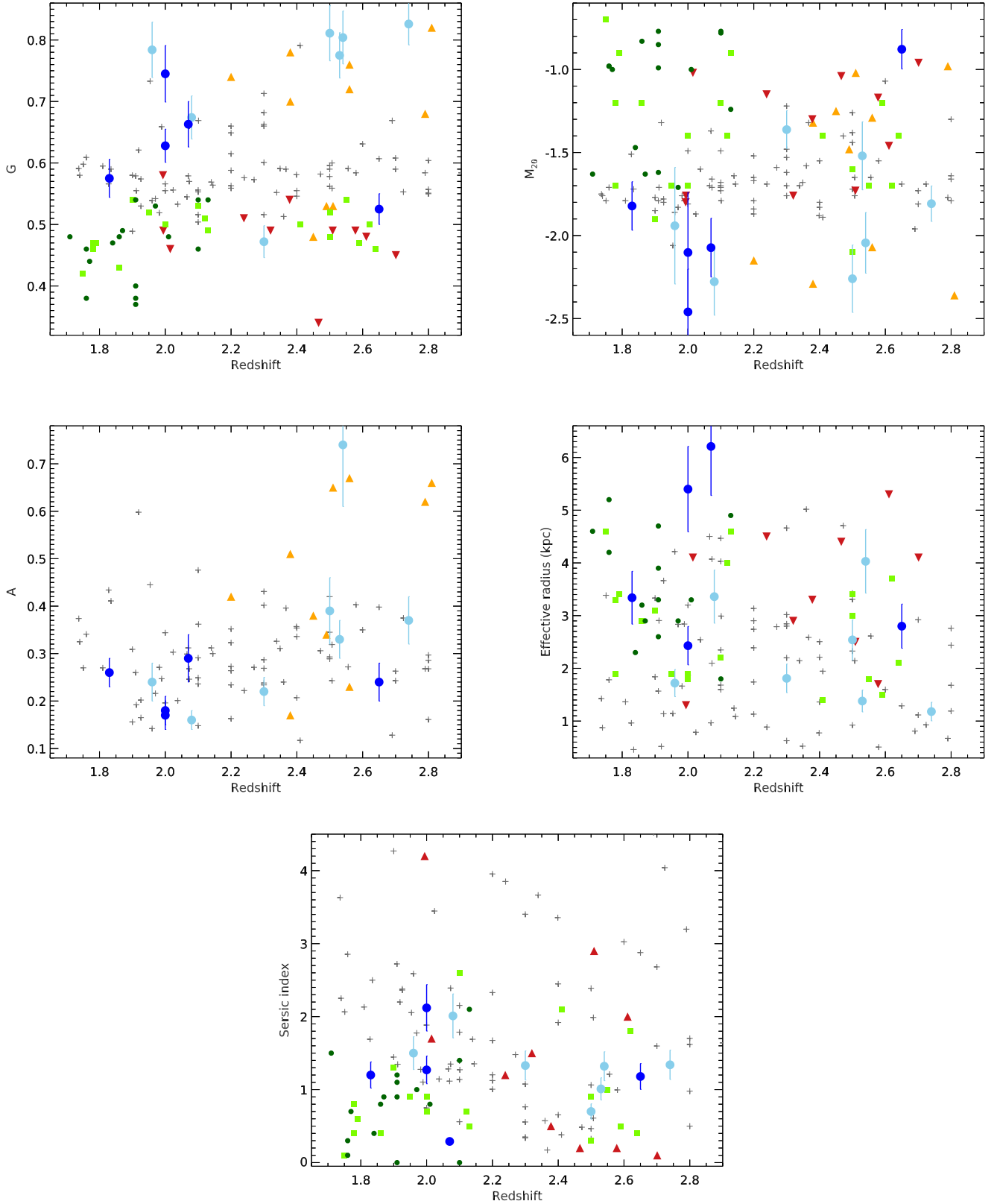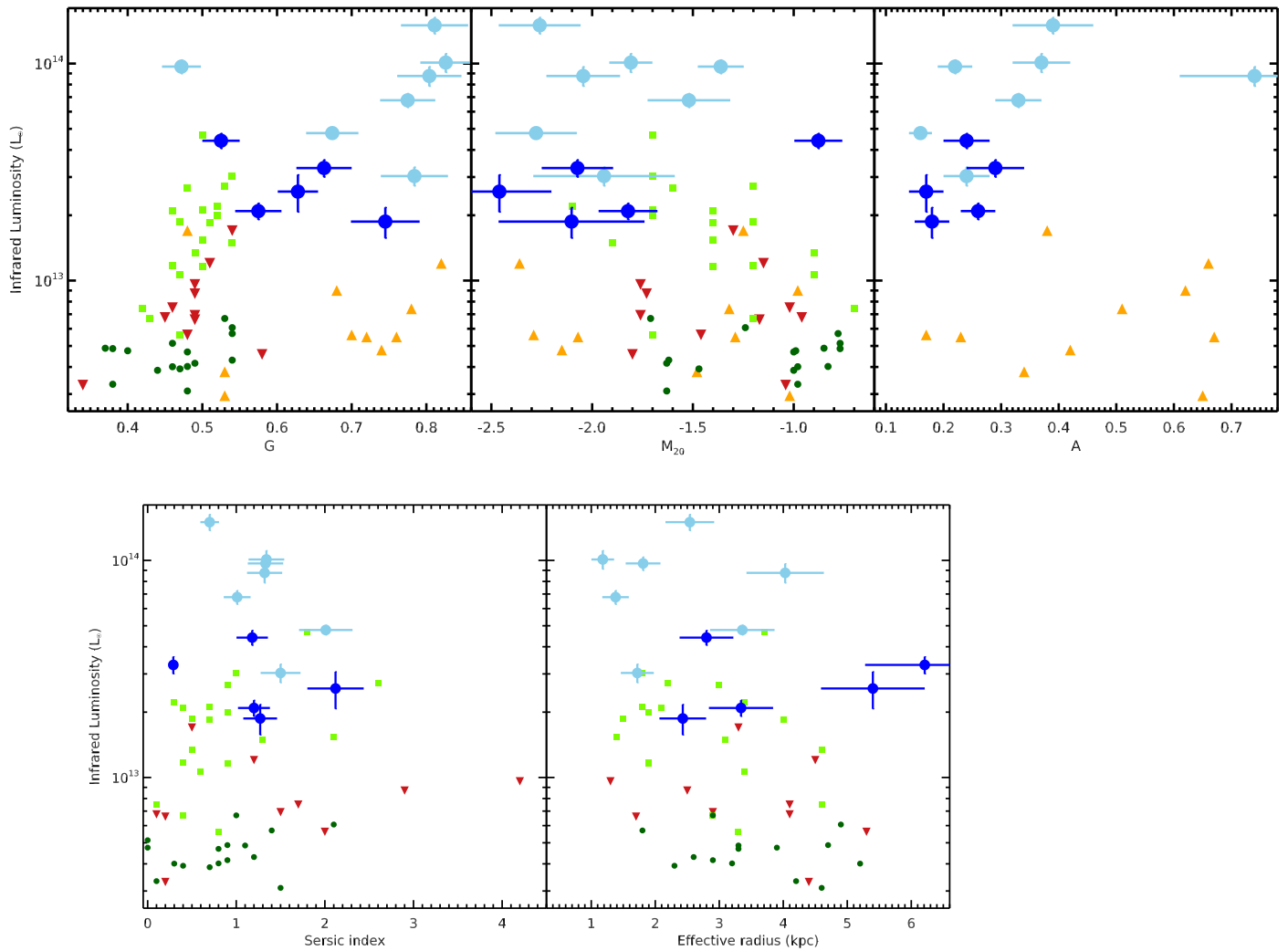
Figure 6. The five morphological parameters of our sample (Section 4.1), plotted as functions of redshift. See Figure 5 for a key to the points and Section 5.1 for a description of the comparison populations.

cut of $A > 0.35$ (Thompson et al. 2015). Using this higher value, no members of our sample are mergers. Using the canonical value (Conselice et al. 2003), only three members of our sample are mergers.

A plausible alternate scenario is as follows. In a massive star-forming galaxy at $z \sim 2$, a luminous AGN raises G and lowers M_{20} relative to the massive star-forming galaxy population but does not appreciably affect A, r_e, or n. This

Figure 7. The five morphological parameters of our sample, plotted as functions of infrared luminosity. See Figure 5 for a key to the points and Section 5.1 for a description of the comparison populations.

scenario is compatible with the work of Pierce et al. (2010), who showed that an AGN can elevate G by up to 0.2 and reduce M_{20} by up to 1.0 while leaving A and n unchanged (see also Simmons & Urry 2008). Such a briefly luminous, or "flickering," AGN placed pseudo-randomly within the massive galaxy population at $z \sim 2$ would also give no correlation between morphologies and AGN fractional luminosities, as we observe.[16]

This scenario implies that the nuclear H-band light arises at least in part from the AGN. Even if this is not the case, this scenario is still plausible. It has been suggested that quenching correlates most strongly with central ($\lesssim 1$ kpc) stellar mass surface density, rather than total stellar mass or Sérsic index (Cheung et al. 2012). Thus, if the G–M_{20} positions of the hDOGs do not arise from AGN light but rather from the earliest formation stages of a bulge, then this could be evidence for such a transition and could link hDOGs to the small fraction of bulge-dominated star-forming galaxies at $z \sim 2$ (Bruce et al. 2014a), as well as SMGs (Simpson et al. 2015). If so, however, it still does not argue for a preferential association with mergers.

This scenario is consistent with studies that propose that mergers are not the main mode for massive galaxy assembly at $z \gtrsim 2$ (Wang et al. 2012; Lofthouse et al. 2017), nor are they the only trigger for AGNs, even at high luminosities (Villforth et al. 2014, 2017). For example, it has been suggested that there exist two "channels" for bulge assembly in massive galaxies: (1) a rapid channel at $z > 3$, since some bulges are already in place with high Sérsic indices at $z = 2.5$; and (2) a gradual channel, transitioning from clumpy disks to bulge+disk systems, at $1 < z < 3$ (Huertas-Company et al. 2015). The morphologies of the hDOGs are consistent with this second track. Moreover, Brennan et al. (2015) proposed that models that include a channel for bulge growth via disk instabilities agree better with observations than models in which bulges can grow only through mergers. Furthermore, SMGs may not be exclusively mergers but instead include "extreme" examples of normal star-forming galaxies (Targett et al. 2013). Finally, Schawinski et al. (2012) proposed that only a small fraction of DOGs are mergers, with most being disklike.[17] Finally, this scenario is consistent with that suggested by Cimatti et al. (2013) for lower-luminosity AGNs

---

[16] The ubiquity of mergers in luminous obscured AGNs at $z \lesssim 0.4$ (e.g., Farrah et al. 2001) may seem inconsistent with this, but this could arise due to, e.g., less rapid dark matter density contrast evolution or a lower free gas fraction, thus requiring specific mechanisms to trigger luminous activity.

[17] However, they did suggest that there may be a higher fraction of mergers at high luminosities.
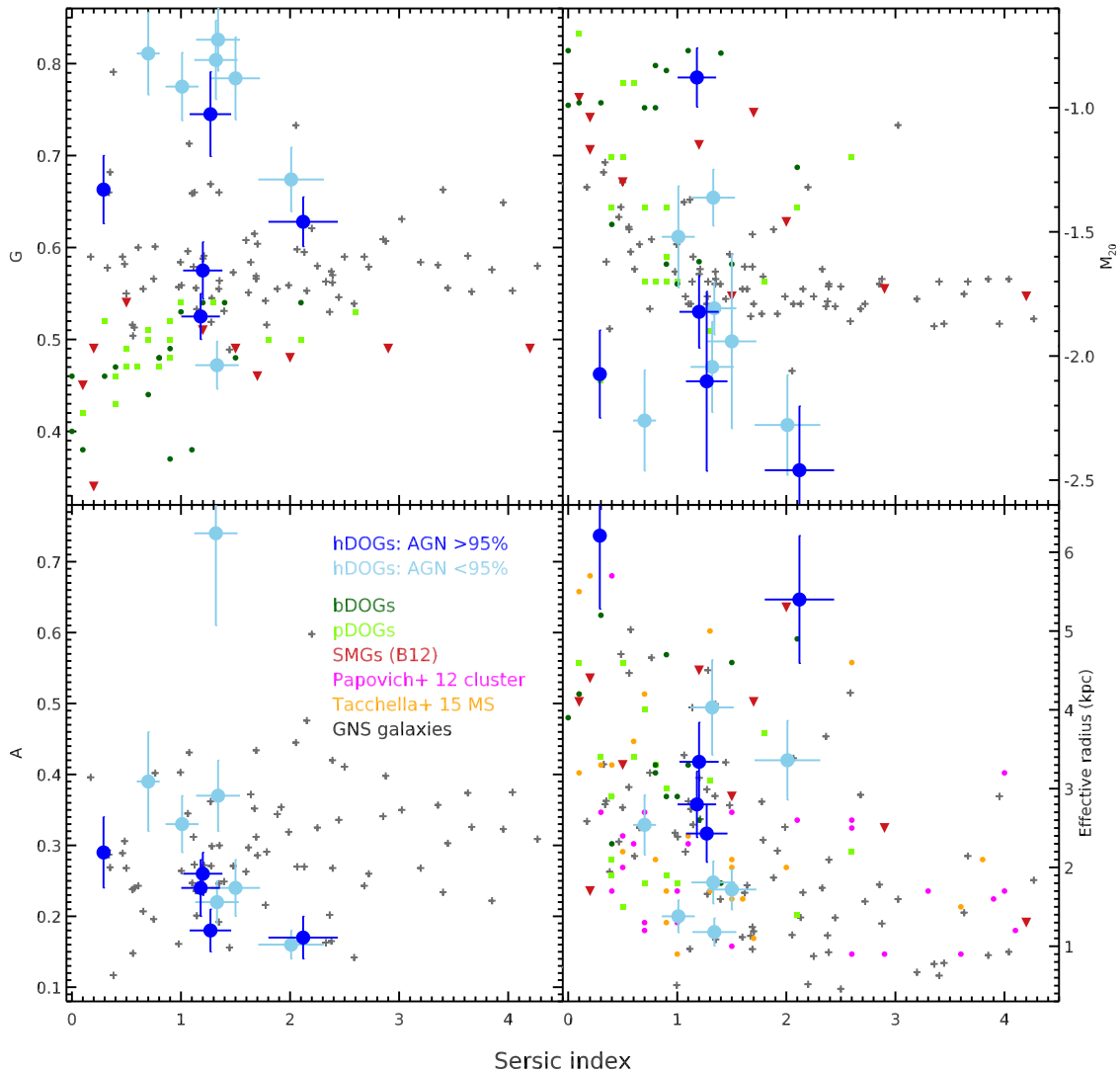
Figure 8. The G, M_{20}, A, and r_e values for our sample, plotted as functions of Sérsic index. See Sections 5.1 and 5.4 for a description of the comparison populations.

at redshifts similar to those of our sample. Thus, even if we posit that hDOGs lie on the same evolutionary path as one or more SMGs, pDOGs, and bDOGs, it is still not necessary to invoke a preference for mergers. The hDOGs can still be the ancestors of low-redshift massive ellipticals, since there is evidence for multistage formation in this population (Petty et al. 2013). There is also no tension with the properties of extremely red quasars (ERQs) at $z \gtrsim 1$; the ERQs show evidence of powerful outflows, and some fraction of the ERQs have colors similar to those of the DOGs (Ross et al. 2015; Hamann et al. 2017), but the ERQs with merging hosts could be the fraction of obscured AGNs that are triggered by mergers.

Overall, with the caveat that our sample is small, we find the second scenario more convincing. We thus conclude that hDOGs are, as a class, a brief and/or rare stage in massive galaxy assembly at $z > 2$, but that they are most likely a phase in which a luminous AGN turns on in a massive star-forming galaxy. Depending on the origin of the nuclear H-band light, this phase may also include the earliest formation stages of a bulge. We do not, however, find that hDOGs are preferentially mergers. This is in contrast to the conclusions drawn by Fan et al. (2016). A significant merger fraction is, however, still plausible, since the $1 < z < 3$ epoch exhibits a higher merger

fraction than do lower redshifts (Lotz et al. 2011), and star formation may be triggered by mergers in up to 27% of massive galaxies at $z = 2$ (Kaviraj et al. 2013).

Finally, we speculate on a link between hDOGs and compact star-forming galaxies. Barro et al. (2014) found that nearly half of all compact $>10^{10} M_\odot$ star-forming galaxies at redshifts similar to those of our sample host an AGN with $L_X \gtrsim 10^{43}$ erg s^{-1}. This fraction of sources that host an AGN is lower than that found in hDOGs but higher than that in main-sequence star-forming galaxies at $z \sim 2$. Moreover, the Sérsic indices of these compact galaxies are similar to those of our sample. It is thus plausible that our sample is the immediate antecedent of the compact star-forming and quiescent galaxies that peak in number at $z \sim 2$. This idea is also consistent with hDOGs not being preferentially associated with mergers, since the dissipational events that lead to compaction can be either gas-rich mergers or disk instabilities triggered by gas accretion (Hopkins et al. 2008; Dekel et al. 2009; Wellons et al. 2015). Moreover, Williams et al. (2014) found that the morphologies of compact early-type galaxies at $z = 1.6$ are inconsistent with a major merger origin. If this is the case, then it may mean that AGNs are important in compacting galaxies at high redshift (Fan et al. 2008, 2010;
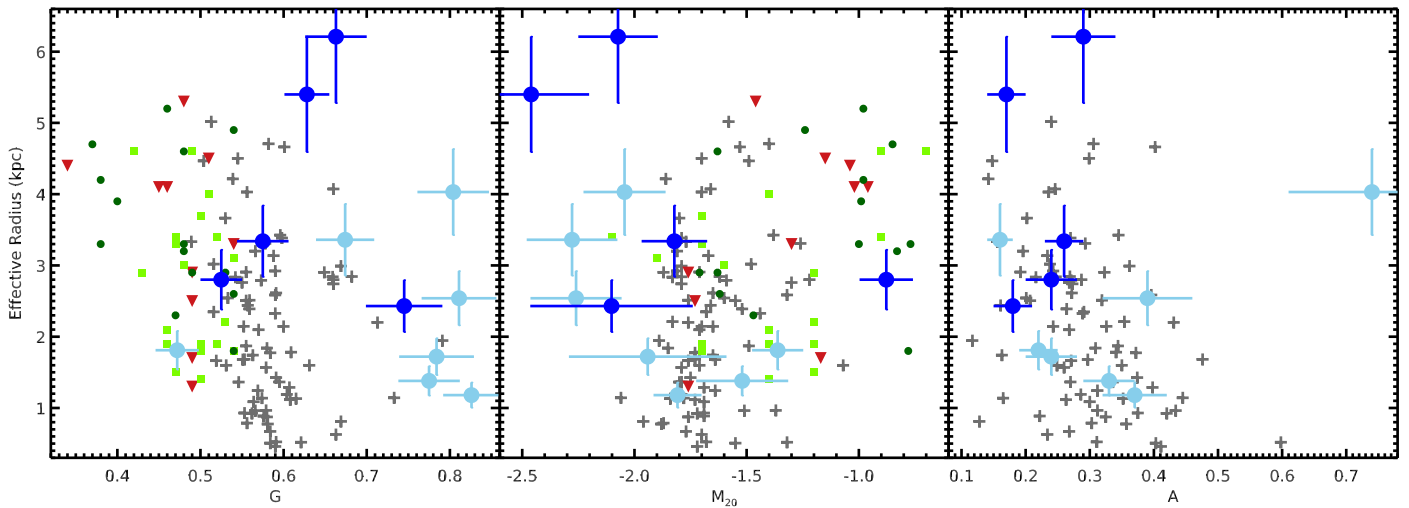
Figure 9. The G, M_{20}, and A values for our sample, plotted as a function of effective radius. See Figure 5 for a key to the points and Section 5.1 for a description of the comparison populations.

Chang et al. 2017; though see also Lilly & Carollo 2016), which would allow for compaction before a galaxy loses the bulk of its gas and dust, as found by Barro et al. (2014). However, since the Barro et al. sample is approximately four orders of magnitude more numerous on the sky than the hDOGs, and their AGNs are at least three orders of magnitude less luminous than those in the hDOGs, our sample could only represent a tiny fraction of the antecedents of compact star-forming galaxies.

7. Conclusions

We have presented *HST* WFC3 F160W imaging and fits to the infrared spectral energy distributions for 12 extremely luminous, obscured AGNs at $1.8 < z < 2.7$. Our conclusions are as follows.

1. The infrared luminosities of our sample lie in the range $(2-15) \times 10^{13} L_{\odot}$, making them among the most luminous objects in the universe at $z \sim 2$. In all cases, the infrared colors and SED fits are consistent with the infrared emission arising at least for the most part from obscured AGN activity. Star formation rates of up to several hundred $M_{\odot}$ yr^{-1} are, however, still plausible in most objects. The AGN fractional luminosities are higher than those seen in selected via either submillimeter emission or an R–24 μm color cut.

2. The morphologies of our sample, sampling rest-frame B-band light, appear mostly clumpy and irregular. Their Gini coefficients span $0.47 < G < 0.81$, their M_{20} parameters nearly all lie in the range $-2.5 < M_{20} < -1.3$, and their asymmetries are nearly all in the range $0.16 < A < 0.39$. These numbers are consistent with our sample being moderately asymmetric but with markedly concentrated and regular light profiles in their central regions. The effective radii of our sample span 1–6 kpc, making them comparable in size to those of near-infrared selected massive galaxies at $z \sim 2$. We see no dependence of AGN luminosity or fractional luminosity on G, M_{20}, A, n, or r_e.

3. The Sérsic indices of our sample span $0.25 < n < 2.15$. Combined with spectroscopic black hole mass measurements from Wu et al. (2017), this is consistent with the

mass assembly of the central black holes in our sample leading the mass assembly of any bulge component.

4. Based on canonical classification boundaries in the G–M_{20}–A plane, most members of our sample are mergers. We do not, however, believe that this is the most plausible scenario. Our sample has asymmetries, effective radii, and Sérsic indices comparable to those of main-sequence star-forming galaxies at $z \sim 2$. Together with the lack of trends between morphological parameters and AGN properties, this implies that our sample is drawn from the massive star-forming galaxies at $z \sim 2$ that harbor a briefly luminous, "flickering" AGN and potentially the earliest formation stages of a bulge in an inside-out manner. While a significant merger fraction is still plausible, we find no need to invoke a preferential link with mergers. The divergent G and M_{20} values of our sample compared to those of massive star-forming galaxies at $z \sim 2$ can also be explained via observed-frame near-infrared emission in the central regions either from the AGN or from a nascent bulge component.

5. We speculate that our sample may represent a small fraction of the immediate antecedents to compact star-forming galaxies at $z \lesssim 2$. The compact galaxies have a lower AGN fraction than our sample but higher than that observed in extended star-forming galaxies at $z > 2$. Moreover, they have Sérsic indices comparable to those of our sample. If the AGNs in our sample are responsible for triggering compaction, and potentially also the formation of a bulge, then this would help explain why compact star-forming galaxies can still harbor large masses of gas and dust.

References

Abraham, R. G., Valdes, F., Yee, H. K. C., & van den Bergh, S. 1994, ApJ, 432, 75

Abraham, R. G., van den Bergh, S., & Nair, P. 2003, ApJ, 588, 218

Aguirre, P., Baker, A. J., Menanteau, F., Lutz, D., & Tacconi, L. J. 2013, ApJ, 768, 164

Alaghband-Zadeh, S., Chapman, S. C., Swinbank, A. M., et al. 2012, MNRAS, 424, 2232

Alatalo, K., Appleton, P. N., Lisenfeld, U., et al. 2015, ApJ, 812, 117

Alexander, D. M., Bauer, F. E., Chapman, S. C., et al. 2005, ApJ, 632, 736

Andreon, S. 2013, A&A, 554, A79

Assef, R. J., Eisenhardt, P. R. M., Stern, D., et al. 2015, ApJ, 804, 27

Assef, R. J., Stern, D., Kochanek, C. S., et al. 2013, ApJ, 772, 26

Barro, G., Faber, S. M., Pérez-González, P. G., et al. 2014, ApJ, 791, 52

Baugh, C. M., Lacey, C. G., Frenk, C. S., et al. 2005, MNRAS, 356, 1191

Bell, E. F., van der Wel, A., Papovich, C., et al. 2012, ApJ, 753, 167

Bertin, E., & Arnouts, S. 1996, A&AS, 117, 393

Béthermin, M., Le Floc'h, E., Ilbert, O., et al. 2012, A&A, 542, A58

Bower, R. G., Benson, A. J., Malbon, R., et al. 2006, MNRAS, 370, 645

Brennan, R., Pandya, V., Somerville, R. S., et al. 2015, MNRAS, 451, 2933

Bridge, C. R., Appleton, P. N., Conselice, C. J., et al. 2007, ApJ, 659, 931

Bridge, C. R., Blain, A., Borys, C. J. K., et al. 2013, ApJ, 769, 91

Bruce, V. A., Dunlop, J. S., McLure, R. J., et al. 2014a, MNRAS, 444, 1001

Bruce, V. A., Dunlop, J. S., McLure, R. J., et al. 2014b, MNRAS, 444, 1660

Bruzual, G., & Charlot, S. 2003, MNRAS, 344, 1000

Buitrago, F., Trujillo, I., Conselice, C. J., et al. 2008, ApJL, 687, L61

Bussmann, R. S., Dey, A., Armus, L., et al. 2012, ApJ, 744, 150

Bussmann, R. S., Dey, A., Lotz, J., et al. 2009, ApJ, 693, 750

Bussmann, R. S., Dey, A., Lotz, J., et al. 2011, ApJ, 733, 21

Caon, N., Capaccioli, M., & D'Onofrio, M. 1993, MNRAS, 265, 1013

Casey, C. M., Narayanan, D., & Cooray, A. 2014, PhR, 541, 45

Chakrabarti, S., Fenner, Y., Cox, T. J., Hernquist, L., & Whitney, B. A. 2008, ApJ, 688, 972

Chang, Y.-Y., Le Floc'h, E., Juneau, S., et al. 2017, MNRAS, 466, L103

Chapman, S. C., Blain, A. W., Smail, I., & Ivison, R. J. 2005, ApJ, 622, 772

Chen, C., Smail, I., Swinbank, A. M., et al. 2015, ApJ, 799, 194

Cheung, E., Faber, S. M., Koo, D. C., et al. 2012, ApJ, 760, 131

Cimatti, A., Brusa, M., Talia, M., et al. 2013, ApJL, 779, L13

Connolly, A. J., Szalay, A. S., Dickinson, M., SubbaRao, M. U., & Brunner, R. J. 1997, ApJL, 486, L11

Conselice, C. J., Bershady, M. A., Dickinson, M., & Papovich, C. 2003, AJ, 126, 1183

Conselice, C. J., Bershady, M. A., & Jangren, A. 2000, ApJ, 529, 886

Conselice, C. J., Bluck, A. F. L., Buitrago, F., et al. 2011, MNRAS, 413, 80

Croft, S., van Breugel, W., de Vries, W., et al. 2006, ApJ, 647, 1040

Croton, D. J., Springel, V., White, S. D. M., et al. 2006, MNRAS, 365, 11

Cushing, M. C., Kirkpatrick, J. D., Gelino, C. R., et al. 2011, ApJ, 743, 50

Cutri, R. M., et al. 2014, yCat, 2328, 0

Daddi, E., Renzini, A., Pirzkal, N., et al. 2005, ApJ, 626, 680

Davé, R., Finlator, K., Oppenheimer, B. D., et al. 2010, MNRAS, 404, 1355

De Young, D. S. 1989, ApJL, 342, L59

Dekel, A., & Birnboim, Y. 2006, MNRAS, 368, 2

Dekel, A., Sari, R., & Ceverino, D. 2009, ApJ, 703, 785

Delvecchio, I., Gruppioni, C., Pozzi, F., et al. 2014, MNRAS, 439, 2736

Dey, A., Soifer, B. T., Desai, V., et al. 2008, ApJ, 677, 943

Di Matteo, T., Springel, V., & Hernquist, L. 2005, Natur, 433, 604

Dickinson, M., Papovich, C., Ferguson, H. C., & Budavári, T. 2003, ApJ, 587, 25

Draper, A. R., & Ballantyne, D. R. 2012, ApJ, 751, 72

Efstathiou, A., Christopher, N., Verma, A., & Siebenmorgen, R. 2013, MNRAS, 436, 1873

Efstathiou, A., & Rowan-Robinson, M. 1995, MNRAS, 273, 649

Efstathiou, A., Rowan-Robinson, M., & Siebenmorgen, R. 2000, MNRAS, 313, 734

Efstathiou, A., & Siebenmorgen, R. 2009, A&A, 502, 541

Eisenhardt, P. R. M., Wu, J., Tsai, C.-W., et al. 2012, ApJ, 755, 173

Fabian, A. C. 2012, ARA&A, 50, 455

Fan, L., Han, Y., Fang, G., et al. 2016, ApJL, 822, L32

Fan, L., Lapi, A., Bressan, A., et al. 2010, ApJ, 718, 1460

Fan, L., Lapi, A., De Zotti, G., & Danese, L. 2008, ApJL, 689, L101

Farrah, D., Afonso, J., Efstathiou, A., et al. 2003, MNRAS, 343, 585

Farrah, D., Baloković, M., Stern, D., et al. 2016, ApJ, 831, 76

Farrah, D., Connolly, B., Connolly, N., et al. 2009, ApJ, 700, 395

Farrah, D., Lebouteiller, V., Spoon, H. W. W., et al. 2013, ApJ, 776, 38

Farrah, D., Rowan-Robinson, M., Oliver, S., et al. 2001, MNRAS, 326, 1333

Farrah, D., Serjeant, S., Efstathiou, A., Rowan-Robinson, M., & Verma, A. 2002, MNRAS, 335, 1163

Farrah, D., Urrutia, T., Lacy, M., et al. 2012, ApJ, 745, 178

Fazio, G. G., Hora, J. L., Allen, L. E., et al. 2004, ApJS, 154, 10

Fiacconi, D., Feldmann, R., & Mayer, L. 2015, MNRAS, 446, 1957

Förster Schreiber, N. M., Genzel, R., Lehnert, M. D., et al. 2006, ApJ, 645, 1062

Förster Schreiber, N. M., Shapley, A. E., Erb, D. K., et al. 2011, ApJ, 731, 65

Gaibler, V., Khochfar, S., Krause, M., & Silk, J. 2012, MNRAS, 425, 438

Genel, S., Genzel, R., Bouché, N., et al. 2008, ApJ, 688, 789

Genzel, R., Lutz, D., Sturm, E., et al. 1998, ApJ, 498, 579

Glikman, E., Simmons, B., Mailly, M., et al. 2015, ApJ, 806, 218

Graham, A. W., & Driver, S. P. 2007, ApJ, 655, 77

Griffin, M. J., Abergel, A., Abreu, A., et al. 2010, A&A, 518, L3

Griffith, R. L., Tsai, C.-W., Stern, D., et al. 2011, ApJL, 736, L22

Haan, S., Surace, J. A., Armus, L., et al. 2011, AJ, 141, 100

Hagen, A., Zeimann, G. R., Behrens, C., et al. 2016, ApJ, 817, 79

Hamann, F., Zakamska, N. L., Ross, N., et al. 2017, MNRAS, 464, 3431

Harris, K., Farrah, D., Schulz, B., et al. 2016, MNRAS, 457, 4179

Hayward, C. C., Kereš, D., Jonsson, P., et al. 2011, ApJ, 743, 159

Hayward, C. C., Narayanan, D., Kereš, D., et al. 2013, MNRAS, 428, 2529

Hernán-Caballero, A., Pérez-Fournon, I., Hatziminaoglou, E., et al. 2009, MNRAS, 395, 1695

Hernquist, L. 1990, ApJ, 356, 359

Hilbert, B., Chiaberge, M., Kotyla, J. P., et al. 2016, ApJS, 225, 12

Holmes, C. C., Caron, F., Griffin, J. E., & Stephens, D. A. 2015, BayAn, 10, 297

Hopkins, A. M., & Beacom, J. F. 2006, ApJ, 651, 142

Hopkins, P. F., Cox, T. J., Kereš, D., & Hernquist, L. 2008, ApJS, 175, 390

Hopkins, P. F., Younger, J. D., Hayward, C. C., Narayanan, D., & Hernquist, L. 2010, MNRAS, 402, 1693

Houck, J. R., Schneider, D. P., Danielson, G. E., et al. 1985, ApJL, 290, L5

Huertas-Company, M., Bernardi, M., Pérez-González, P. G., et al. 2016, MNRAS, 462, 4495

Huertas-Company, M., Pérez-González, P. G., Mei, S., et al. 2015, ApJ, 809, 95

Hung, C.-L., Sanders, D. B., Casey, C. M., et al. 2014, ApJ, 791, 63

Iglesias-Páramo, J., Buat, V., Hernández-Fernández, J., et al. 2007, ApJ, 670, 279

Ishibashi, W., Fabian, A. C., & Canning, R. E. A. 2013, MNRAS, 431, 2350

Ivison, R. J., Smail, I., Amblard, A., et al. 2012, MNRAS, 425, 1320

Jones, S. F., Blain, A. W., Lonsdale, C., et al. 2015, MNRAS, 448, 3325

Jones, S. F., Blain, A. W., Stern, D., et al. 2014, MNRAS, 443, 146

Kartaltepe, J., Dickinson, M., Alexander, D. M., et al. 2012, ApJ, 757, 23

Kartaltepe, J., Sanders, D. B., Le Floc'h, E., et al. 2010, ApJ, 721, 98

Kartaltepe, J. S., Mozena, M., Kocevski, D., et al. 2015, ApJS, 221, 11

Kaviraj, S., Cohen, S., Windhorst, R. A., et al. 2013, MNRAS, 429, L40

Kereš, D., Katz, N., Davé, R., Fardal, M., & Weinberg, D. H. 2009, MNRAS, 396, 2332

King, A. 2005, ApJL, 635, L121

Kocevski, D. D., Brightman, M., Nandra, K., et al. 2015, ApJ, 814, 104

Lacy, M., Wilson, G., Masci, F., et al. 2005, ApJS, 161, 41

Lagache, G., Puget, J.-L., & Dole, H. 2005, ARA&A, 43, 727

Lang, P., Wuyts, S., Somerville, R. S., et al. 2014, ApJ, 788, 11

Lanzetta, K. M., Yahata, N., Pascarelle, S., Chen, H.-W., & Fernández-Soto, A. 2002, ApJ, 570, 492

Lauer, T. R., Ajhar, E. A., Byun, Y.-I., et al. 1995, AJ, 110, 2622

Lee, B., Giavalisco, M., Williams, C. C., et al. 2013, ApJ, 774, 47

Le Floc'h, E., Papovich, C., Dole, H., et al. 2005, ApJ, 632, 169

Lilly, S. J., & Carollo, C. M. 2016, ApJ, 833, 1

Lilly, S. J., Le Fevre, O., Hammer, F., & Crampton, D. 1996, ApJL, 460, L1

Lofthouse, E. K., Kaviraj, S., Conselice, C. J., Mortlock, A., & Hartley, W. 2017, MNRAS, 465, 2895

Lonsdale, C. J., Farrah, D., & Smith, H. E. 2006, in Astrophysics Update 2, ed. J. W. Mason (Chichester: Praxis Publishing Ltd)

Lonsdale, C. J., Lacy, M., Kimball, A. E., et al. 2015, ApJ, 813, 45
Lotz, J. M., Davis, M., Faber, S. M., et al. 2008a, ApJ, 672, 177
Lotz, J. M., Jonsson, P., Cox, T. J., et al. 2011, ApJ, 742, 103
Lotz, J. M., Jonsson, P., Cox, T. J., & Primack, J. R. 2008b, MNRAS, 391, 1137
Lotz, J. M., Madau, P., Giavalisco, M., Primack, J., & Ferguson, H. C. 2006, ApJ, 636, 592
Lotz, J. M., Primack, J., & Madau, P. 2004, AJ, 128, 163
Magorrian, J., Tremaine, S., Richstone, D., et al. 1998, AJ, 115, 2285
Mainieri, V., Bongiorno, A., Merloni, A., et al. 2011, A&A, 535, A80
Mancini, C., Renzini, A., Daddi, E., et al. 2015, MNRAS, 450, 763
Melbourne, J., Bussman, R. S., Brand, K., et al. 2009, AJ, 137, 4854
Melbourne, J., Soifer, B. T., Desai, V., et al. 2012, AJ, 143, 125
Morishita, T., Ichikawa, T., & Kajisawa, M. 2014, ApJ, 785, 18
Morishita, T., Ichikawa, T., Noguchi, M., et al. 2015, ApJ, 805, 34
Mortlock, A., Conselice, C. J., Hartley, W. G., et al. 2013, MNRAS, 433, 1185
Narayanan, D., Turk, M., Feldmann, R., et al. 2015, Natur, 525, 496
Olivares, V., Treister, E., Privon, G. C., et al. 2016, ApJ, 827, 57
Papovich, C., Bassett, R., Lotz, J. M., et al. 2012, ApJ, 750, 93
Peng, C. Y., Ho, L. C., Impey, C. D., & Rix, H.-W. 2002, AJ, 124, 266
Pérez-González, P. G., Rieke, G. H., Egami, E., et al. 2005, ApJ, 630, 82
Petty, S. M., Armus, L., Charmandaris, V., et al. 2014, AJ, 148, 111
Petty, S. M., de Mello, D. F., Gallagher, J. S., III, et al. 2009, AJ, 138, 362
Petty, S. M., Neill, J. D., Jarrett, T. H., et al. 2013, AJ, 146, 77
Pierce, C. M., Lotz, J. M., Primack, J. R., et al. 2010, MNRAS, 405, 718
Pilbratt, G. L., Riedinger, J. R., Passvogel, T., et al. 2010, A&A, 518, L1
Poglitsch, A., Waelkens, C., Geis, N., et al. 2010, A&A, 518, L2
Pope, A., Bussmann, R. S., Dey, A., et al. 2008, ApJ, 689, 127
Psychogyios, A., Charmandaris, V., Diaz-Santos, T., et al. 2016, A&A, 591, A1
Ravindranath, S., Giavalisco, M., Ferguson, H. C., et al. 2006, ApJ, 652, 963
Ricci, C., Bauer, F. E., Treister, E., et al. 2017, MNRAS, 468, 1273
Ricciardelli, E., Trujillo, I., Buitrago, F., & Conselice, C. J. 2010, MNRAS, 406, 230
Richards, G. T., Strauss, M. A., Fan, X., et al. 2006, AJ, 131, 2766
Ross, N. P., Hamann, F., Zakamska, N. L., et al. 2015, MNRAS, 453, 3932
Rowan-Robinson, M. 2000, MNRAS, 316, 885
Sanders, D. B., & Mirabel, I. F. 1996, ARA&A, 34, 749
Savage, R. S., & Oliver, S. 2007, ApJ, 661, 1339
Schawinski, K., Simmons, B. D., Urry, C. M., Treister, E., & Glikman, E. 2012, MNRAS, 425, L61
Sérsic, J. L. 1963, BAAA, 6, 41
Silk, J. 2013, ApJ, 772, 112
Simmons, B. D., & Urry, C. M. 2008, ApJ, 683, 644
Simpson, J. M., Smail, I., Swinbank, A. M., et al. 2015, ApJ, 799, 81
Spoon, H. W. W., Farrah, D., Lebouteiller, V., et al. 2013, ApJ, 775, 127
Stern, D., Assef, R. J., Benford, D. J., et al. 2012, ApJ, 753, 30
Stern, D., Lansbury, G. B., Assef, R. J., et al. 2014, ApJ, 794, 102
Stierwalt, S., Armus, L., Surace, J. A., et al. 2013, ApJS, 206, 1
Surace, J. A., Sanders, D. B., Vacca, W. D., Veilleux, S., & Mazzarella, J. M. 1998, ApJ, 492, 116
Swinbank, A. M., Smail, I., Chapman, S. C., et al. 2010, MNRAS, 405, 234
Tacchella, S., Lang, P., Carollo, C. M., et al. 2015, ApJ, 802, 101
Tacconi, L. J., Neri, R., Genzel, R., et al. 2013, ApJ, 768, 74
Taniguchi, Y., Kajisawa, M., Kobayashi, M. A. R., et al. 2015, ApJL, 809, L7
Targett, T. A., Dunlop, J. S., Cirasuolo, M., et al. 2013, MNRAS, 432, 2012
Targett, T. A., Dunlop, J. S., McLure, R. J., et al. 2011, MNRAS, 412, 295
Thompson, R., Davé, R., Huang, S., & Katz, N. 2015, arXiv:1508.01851
Treister, E., Schawinski, K., Urry, C. M., & Simmons, B. D. 2012, ApJL, 758, L39
Tremaine, S., Gebhardt, K., Bender, R., et al. 2002, ApJ, 574, 740
Tsai, C.-W., Eisenhardt, P. R. M., Wu, J., et al. 2015, ApJ, 805, 90
Urrutia, T., Lacy, M., & Becker, R. H. 2008, ApJ, 674, 80
van Dokkum, P. G., Franx, M., Kriek, M., et al. 2008, ApJL, 677, L5
van Dokkum, P. G., Whitaker, K. E., Brammer, G., et al. 2010, ApJ, 709, 1018
Veilleux, S., Kim, D.-C., & Sanders, D. B. 2002, ApJS, 143, 315
Verma, A., Rowan-Robinson, M., McMahon, R., & Efstathiou, A. 2002, MNRAS, 335, 574
Villforth, C., Hamann, F., Rosario, D. J., et al. 2014, MNRAS, 439, 3342
Villforth, C., Hamilton, T., Pawlik, M. M., et al. 2017, MNRAS, 466, 812
Wall, J. V., Pope, A., & Scott, D. 2008, MNRAS, 383, 435
Wang, L., Farrah, D., Oliver, S. J., et al. 2013, MNRAS, 431, 648
Wang, L., Viero, M., Clarke, C., et al. 2014, MNRAS, 444, 2870
Wang, T., Huang, J.-S., Faber, S. M., et al. 2012, ApJ, 752, 134
Weinzirl, T., Jogee, S., Conselice, C. J., et al. 2011, ApJ, 743, 87
Wellons, S., Torrey, P., Ma, C.-P., et al. 2015, MNRAS, 449, 361
Werner, M. W., Roellig, T. L., Low, F. J., et al. 2004, ApJS, 154, 1
Wiklind, T., Conselice, C. J., Dahlen, T., et al. 2014, ApJ, 785, 111
Williams, C. C., Giavalisco, M., Cassata, P., et al. 2014, ApJ, 780, 1
Wright, E. L., Eisenhardt, P. R. M., Mainzer, A. K., et al. 2010, AJ, 140, 1868
Wu, J., Bussmann, R. S., Tsai, C.-W., et al. 2014, ApJ, 793, 8
Wu, J., Jun, H. D., Assef, R. J., et al. 2017, ApJ, in press (arXiv:1703.06888)
Wu, J., Tsai, C.-W., Sayers, J., et al. 2012, ApJ, 756, 96
Wuyts, S., Förster Schreiber, N. M., Genzel, R., et al. 2012, ApJ, 753, 114
Wuyts, S., Förster Schreiber, N. M., van der Wel, A., et al. 2011, ApJ, 742, 96
Zamojski, M., Yan, L., Dasyra, K., et al. 2011, ApJ, 730, 125
Zubovas, K., Nayakshin, S., King, A., & Wilkinson, M. 2013, MNRAS, 433, 3079